PLOS Computational Biology

RESEARCH ARTICLE

Inward rectifier potassium channels interact with calcium channels to promote robust and physiological bistability

Anaëlle De Worm*, Guillaume Drion☯, Pierre Sacré☯

Department of Electrical Engineering and Computer Science, University of Liège, Liège, Belgium

☯ These authors contributed equally to this work.
* anaelle.deworm@uliege.be

OPEN ACCESS

Citation: De Worm A, Drion G, Sacré P (2026) Inward rectifier potassium channels interact with calcium channels to promote robust and physiological bistability. PLoS Comput Biol 22(7): e1014549. https://doi.org/10.1371/journal.pcbi.1014549

Editor: Hermann Cuntz, Ernst-Strungmann-Institut, GERMANY

Received: May 23, 2025

Accepted: July 8, 2026

Published: July 28, 2026

Peer Review History: PLOS recognizes the benefits of transparency in the peer review process; therefore, we enable the publication of all of the content of peer review and author responses alongside final, published articles. The editorial history of this article is available here: https://doi.org/10.1371/journal.pcbi.1014549

Abstract

Projection neurons in the dorsal horn relay nociceptive input to supraspinal centers. During central sensitization, a subset of them switches from tonic firing to plateau potentials with sustained afterdischarges, a change that requires intrinsic bistability between a resting and a spiking state. Voltage-gated L-type calcium (CaL) channels can produce bistability, but reach physiological resting states only when paired with voltage-gated potassium channels, most of which simultaneously shrink the bistability window. How robust, physiological bistability arises has therefore remained unclear. Using a minimal conductance-based model, we show that inward rectifier potassium (Kir) channels enlarge the bistability window when combined with CaL channels, while M-type potassium (KM) channels slightly reduce it. Within the parameter region where bistability is both robust and physiological, both channel types can sustain bistability, but the CaL + Kir combination produces a substantially larger window and is more robust to noise and intrinsic variability. This window-enlarging effect traces to a shape feature of the outward Kir steady-state current: like the CaL current, it has a region of negative differential conductance around the spike threshold, a feature absent from KM and from most other voltage-gated potassium currents. Bifurcation analysis further shows that the two pairs support qualitatively distinct excitability: plateau-generating bistability for CaL + Kir and resonator-like dynamics for CaL + KM. These conclusions hold in a two-compartment model of deep projection neurons with realistic ion channel complements, and identify the CaL + Kir pair as a candidate intrinsic mechanism for central sensitization.

Author summary

Many neurons can hold two stable states (resting or firing) at the same input current, depending on their recent history. This bistability underlies a form of short-term memory at the single-cell level and appears in contexts as varied as sleep

Data availability statement: All data and code used for running experiments and plotting are available at https://github.com/anadew2/cal-kir-bistability/tree/main.

Funding: This work was supported by the Belgian Government through the Federal Public Service Policy and Support (NEMODEI2 to A.D.W., G.D., and P.S.). Computational resources have been provided (to A.D.W.) by the Consortium des Équipements de Calcul Intensif (CÉCI), funded by the Fonds de la Recherche Scientifique de Belgique (F.R.S.-FNRS) under Grant No. 2.5020.11 and by the Walloon Region. The funders had no role in study design, data collection and analysis, decision to publish, or preparation of the manuscript.

Competing interests: The authors have declared that no competing interests exist.

rhythms, motor control, working memory, and pain signal amplification during central sensitization. How bistability arises in a physiologically plausible way has remained partly unresolved. L-type calcium (CaL) channels generate bistability, but at abnormally low resting states; additional channels must redress these potentials, yet most potassium channels that do so also shrink the range of currents over which bistability exists. Using a conductance-based model, we show that inward rectifier potassium (Kir) channels are more favourable than M-type potassium (KM) channels in this regard: paired with CaL channels, they produce a bistability that is both physiological and stable against noise and cell-to-cell variability over a substantially wider range of parameters than KM channels can. The difference traces to a shape feature of the Kir steady-state current, shared with CaL but absent from most potassium currents. Because Kir channels are regulated by many neuromodulatory pathways in the dorsal horn, the CaL + Kir pair is a candidate mechanism for pain amplification during central sensitization and, more broadly, for single-cell short-term memory.

Introduction

Nociceptive pain protects the body by signaling tissue-damaging stimuli [1]. Under strong or repeated stimulation, sensitization alters the nociceptive system and amplifies pain signaling [2]. In the dorsal horn, projection neurons relay sensory input to supraspinal centers, and sensitization renders a subset of them hyperexcitable [3–5]. Deep projection neurons, in particular, can switch from tonic firing to plateau potentials—a sustained depolarized state interposed between the spiking and resting voltage ranges—with sustained afterdischarges when neuromodulation changes [6]. These afterdischarges substantially increase the signal sent upstream and underlie hyperalgesia [4,7,8]. Because they sustain spiking beyond the end of a stimulus instead of reverting to rest, sustained afterdischarges reveal an intrinsic bistability between resting and spiking states [4].

Neuronal bistability has been observed in many populations [9–14], yet how it emerges in single neurons in a form that is both robust and physiological remains unclear. We call bistability *physiological* when its resting states lie above the potassium reversal potential, as observed in deep projection neurons [6,15,16]; we call it *robust* when the *bistability window*, defined as the range of currents from I_1 (onset of spiking from rest) to I_2 (cessation of resting from spiking), is wide enough that both states are reliably reached. Computational studies show that voltage-gated calcium channels create bistability, but at resting states that become physiological only when these channels are paired with voltage-gated potassium channels [14,17,18]. Most such potassium channels, however, also shrink the bistability window [13,19,20], producing a trade-off between window size and the plausibility of resting states. Inward rectifier potassium (Kir) channels, a distinct subclass expressed in superficial and deep dorsal horn projection neurons [6,21–24], can themselves induce bistability

[25–28]. Whether and how Kir channels interact with calcium channels to shape bistability, and through what mechanism, remain open questions.

Here, we use a *minimal* conductance-based model to show that Kir channels, when coupled with L-type calcium (CaL) channels, enlarge the bistability window, whereas M-type potassium (KM) channels reduce it. We reproduce this effect in a published two-compartment model of deep projection neurons that already includes CaL and Kir channels alongside other currents [29]. The two pairs produce bistabilities that differ in robustness to noise and intrinsic variability; we trace these differences to the contrasting shapes of the Kir and KM steady-state currents, and relate each pair to a distinct excitability switch.

Results

We begin by asking how each channel pair shapes the bistability window in a minimal model, then validate the effect in a two-compartment model. We then quantify the robustness of each bistability to noise and intrinsic variability, tracing the differences to the steady-state shapes of the three currents. Finally, we link each pair to a distinct excitability switch, which unifies the mechanistic and functional observations.

CaL channels drive bistability; KM channels slightly narrow the window while Kir channels enlarge it

To examine how calcium and potassium channels jointly shape bistability, we built a minimal conductance-based model combining a fast sodium current I_{Na}, a delayed-rectifier potassium current I_{KDR}, a leak current I_{leak}, and L-type calcium (CaL) channels, and compared the effect of adding either M-type potassium (KM) or inward rectifier potassium (Kir) channels.

CaL channels alone created a bistability window, but at resting states that fell below the potassium reversal potential. Without CaL channels the minimal model did not exhibit bistability (see S1 Appendix). Adding CaL channels produced bistability between a resting and a spiking state, revealed by applying ascending and descending current steps that reached the same final current (Fig 1A-1B). Indeed, for the two middle currents, the final state depended on the initial behavior (Fig 1A-1B, red tones), while the smallest and largest currents yielded resting or spiking regardless of initial conditions (purple and yellow). The frequency-current (fI) curves obtained from initially resting and initially spiking neurons (see Methods) showed a bistability window of 2.1 μA/cm^2 delimited by I_1 and I_2 (Fig 1C, top). Above I_2, only spiking was observed (Fig 1, yellow marker). From I_1 to I_2, both resting and spiking could be observed depending on the neuron initial conditions (Fig 1, markers in red tones). Only resting was observed for currents below I_1 (Fig 1, purple marker). Throughout, we use $\overline{V}(I)$ to denote the steady-state membrane potential associated with the resting equilibrium at a given applied current I; this is distinct from the conventional resting potential, which refers to the membrane potential in the absence of stimulation. Within this window, $\overline{V}(I)$ fell well below the potassium reversal potential (Fig 1C, bottom), so CaL channels must be combined with other currents to produce physiologically plausible bistability.

Adding an M-type potassium maximal conductance $\bar{g}_{KM}$ redressed the resting equilibria but slightly narrowed the bistability window. With a baseline current below the new I_1, a current pulse elicited a finite afterdischarge: the neuron transitioned to spiking during the pulse and eventually returned to resting after the pulse ended (Fig 2A). The termination of spiking is attributable to the progressive decrease in the CaL current caused by the slow cumulative inactivation of CaL channels during spiking (Fig 2A, bottom). The corresponding fI curves showed a narrower window than without KM channels (Fig 2B, purple, vs. Fig 1C), while $\overline{V}(I)$ within the window approached physiological values (Fig 2C). The stimulation protocols in Fig 2A and Fig 1A–1B are equivalent approaches that can demonstrate bistability. In the pulse protocol, the pulse amplitude must exceed the bistability window to trigger a transition from resting to spiking, while the baseline current must lie within it to sustain the new state. In the ascending/descending step protocol, the pre-step current must fall above I_2 or below I_1 to establish the initial state, while the final current must lie within it to maintain that state.

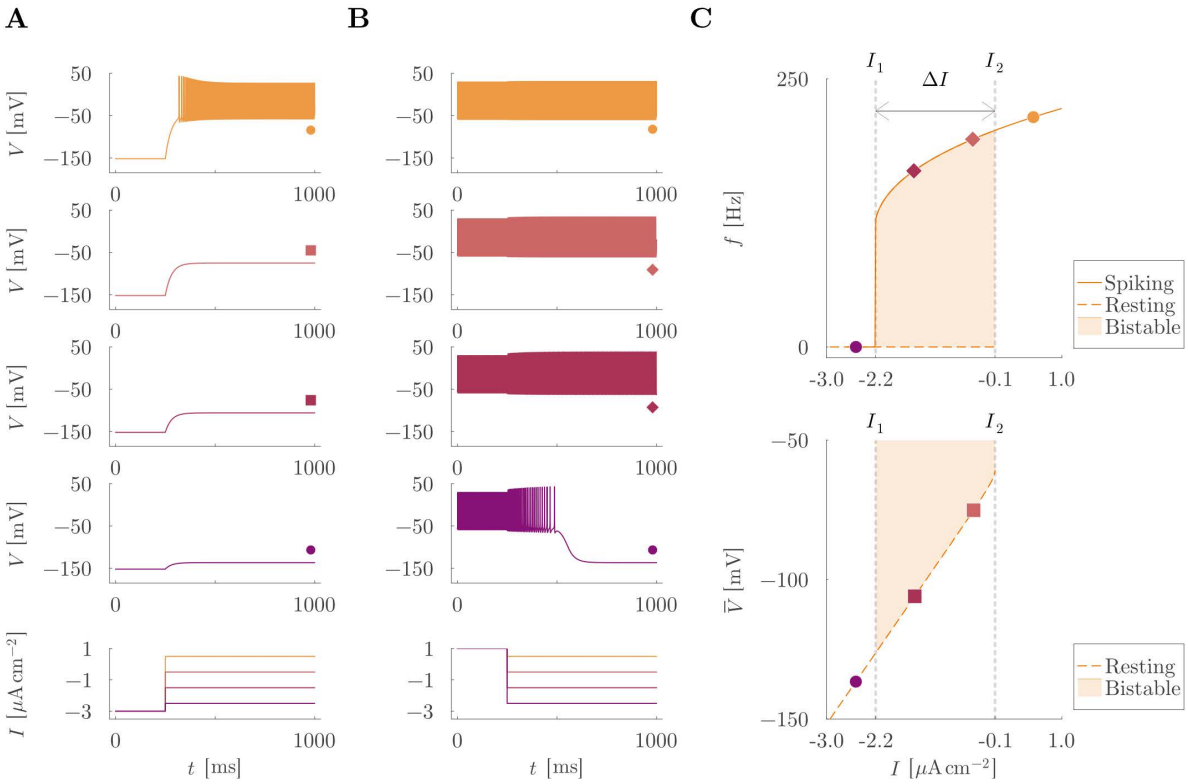

Fig 1. Voltage-gated calcium channels produce bistability between resting and spiking states. A: From an initial resting state, ascending current steps progressively depolarize the membrane (purple and reds). The largest step triggers a switch to spiking (yellow). B: From an initial spiking state, descending current steps progressively decrease the firing frequency (yellow and reds). The largest step triggers a switch to resting (purple). C: The frequency-current (fI) curves obtained from initially resting and initially spiking neurons (top, dashed and solid lines, respectively) identify the bistability window: the current range from I_1 to I_2 in which both states coexist (red tones, matching A and **B**). The resting equilibria, noted $\bar{V}(I)$, depolarize progressively with increasing current (bottom). Markers in A, B, and C identify the final state observed for each of the final applied currents of −2.5, −1.5, −0.5, and 0.5 μA/cm² (from bottom to top).

https://doi.org/10.1371/journal.pcbi.1014549.g001

Replacing KM with an inward rectifier potassium (Kir) conductance $\bar{g}_{Kir}$ preserved the correction of resting equilibria while enlarging the bistability window. A current pulse of the same amplitude and a baseline below I_1 again produced a finite afterdischarge, with the neuron returning to a resting equilibrium of –89 mV (Fig 2D). As with KM channels, spiking termination is attributable to the slow cumulative inactivation of CaL channels (Fig 2D, bottom). The superimposed fI curves showed a larger bistability window than with CaL alone, shifted toward higher currents (Fig 2E). Kir channels also brought $\bar{V}(I)$ within the window to physiological values (Fig 2F).

To see how these effects evolve across the full conductance space, we swept $\bar{p}_{CaL}$ jointly with either $\bar{g}_{KM}$ or $\bar{g}_{Kir}$. A systematic sweep over $\bar{p}_{CaL}$ and $\bar{g}_{KM}$ confirmed the observations above. We computed the bistability window size $\Delta I = I_2 - I_1$, its lower limit I_1, and the resting equilibrium at that limit $\bar{V}(I_1)$ across the two-dimensional parameter space (Fig 3A–3C, respectively). KM channels slightly narrowed the window at high $\bar{p}_{CaL}$: with $\bar{p}_{CaL} = 1.725 \times 10^{-5}$ cm s^{-1}, raising $\bar{g}_{KM}$ to 0.3 mS/cm² reduced ΔI from 2.7 to 2.3 μA/cm² (Fig 3A). For lower $\bar{p}_{CaL}$, KM channels slightly enlarged ΔI, but only in parameter regions where bistability was neither robust ($\Delta I < 1.6$ μA/cm²) nor physiological ($\bar{V}(I_1) < -90$ mV). KM channels raised both I_1 (Fig 3B) and $\bar{V}(I_1)$ steeply, with $\bar{V}(I_1)$ reaching values above –60 mV (Fig 3C, blue area); this depolarization already hints at an excitability change driven by KM recruitment, which we examine later.

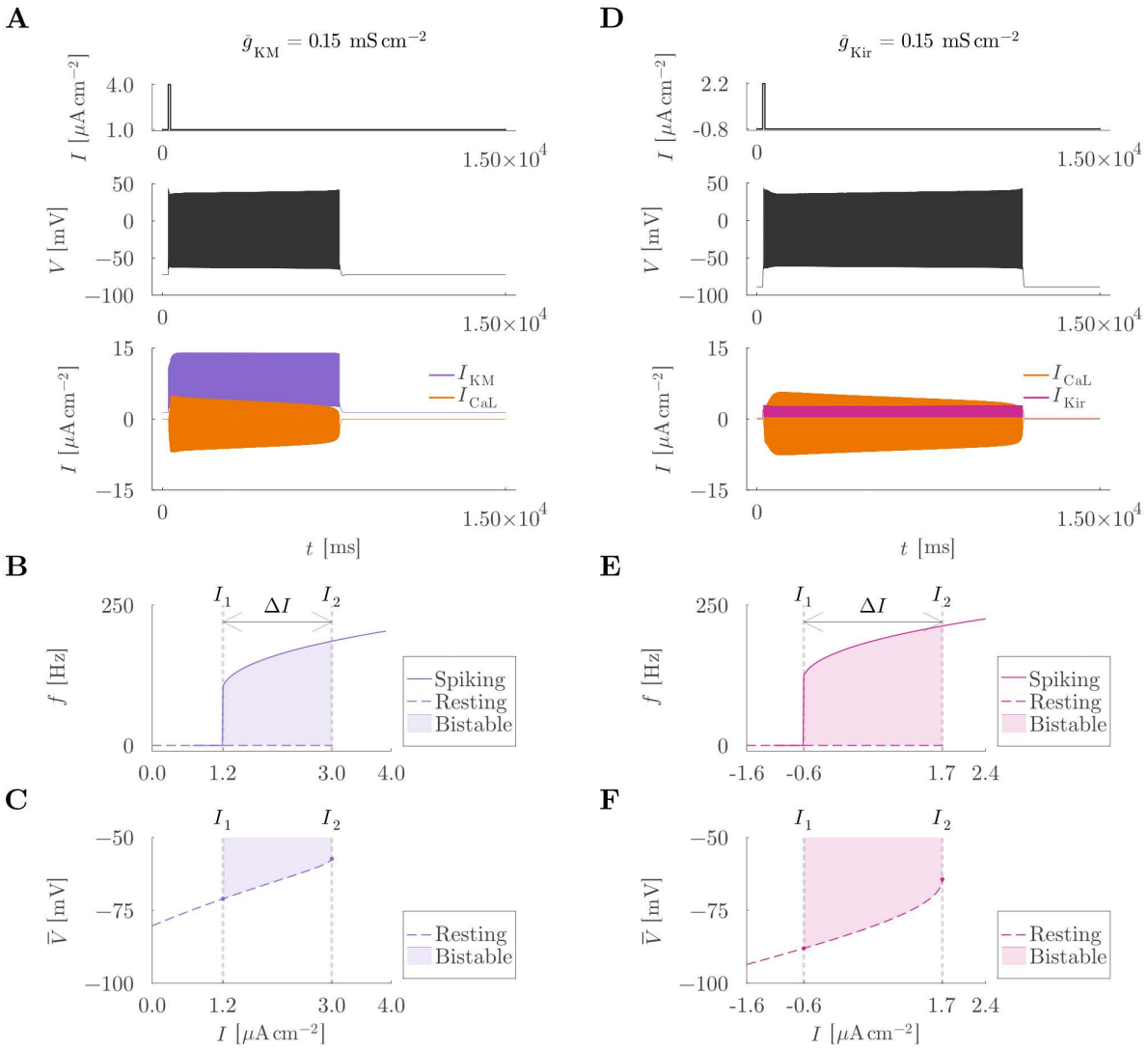

Fig 2. Both KM and Kir channels redress the resting equilibria, and modulate bistability. A: After adding an M-type potassium conductance $\bar{g}_{KM}$, a current pulse from a baseline below I_1 elicits a finite afterdischarge: the neuron spikes during the pulse and returns to rest afterwards (top). The I_{CaL} and I_{KM} traces show that I_{CaL} declines during spiking, eventually terminating it (bottom). B: The fI curves show that the bistability window created by CaL channels (Fig 1C, top) slightly narrows after adding KM channels. C: The resting equilibria within the window, originally below E_K (Fig 1C, bottom), are redressed by KM channels. D: After replacing KM with an inward rectifier potassium conductance $\bar{g}_{Kir}$, a current pulse from a baseline below the new I_1 again elicits a finite afterdischarge. E: The bistability window is preserved after adding Kir channels. F: Kir channels also redress the resting equilibria within the window.

https://doi.org/10.1371/journal.pcbi.1014549.g002

In contrast to this small narrowing effect, a sweep over $\bar{p}_{CaL}$ and $\bar{g}_{Kir}$ showed that Kir channels enlarge the bistability window while anchoring the resting equilibria. For any $\bar{p}_{CaL}$, raising $\bar{g}_{Kir}$ increased both ΔI and I_1, and held $\bar{V}(I_1)$ close to –75 mV (Fig 3D–3F, respectively). These effects of CaL, KM, and Kir channels on window size were independent of the specific CaL current model used (see S2 Appendix). The contrasting behaviors of the CaL + KM and CaL + Kir pairs suggest that each relies on a distinct mechanism and may drive a distinct excitability switch, which we return to later.

A natural question is whether these effects are still observed when KM and Kir are expressed simultaneously. When KM and Kir channels were combined with CaL channels together, each retained its distinct effect. Starting from a baseline

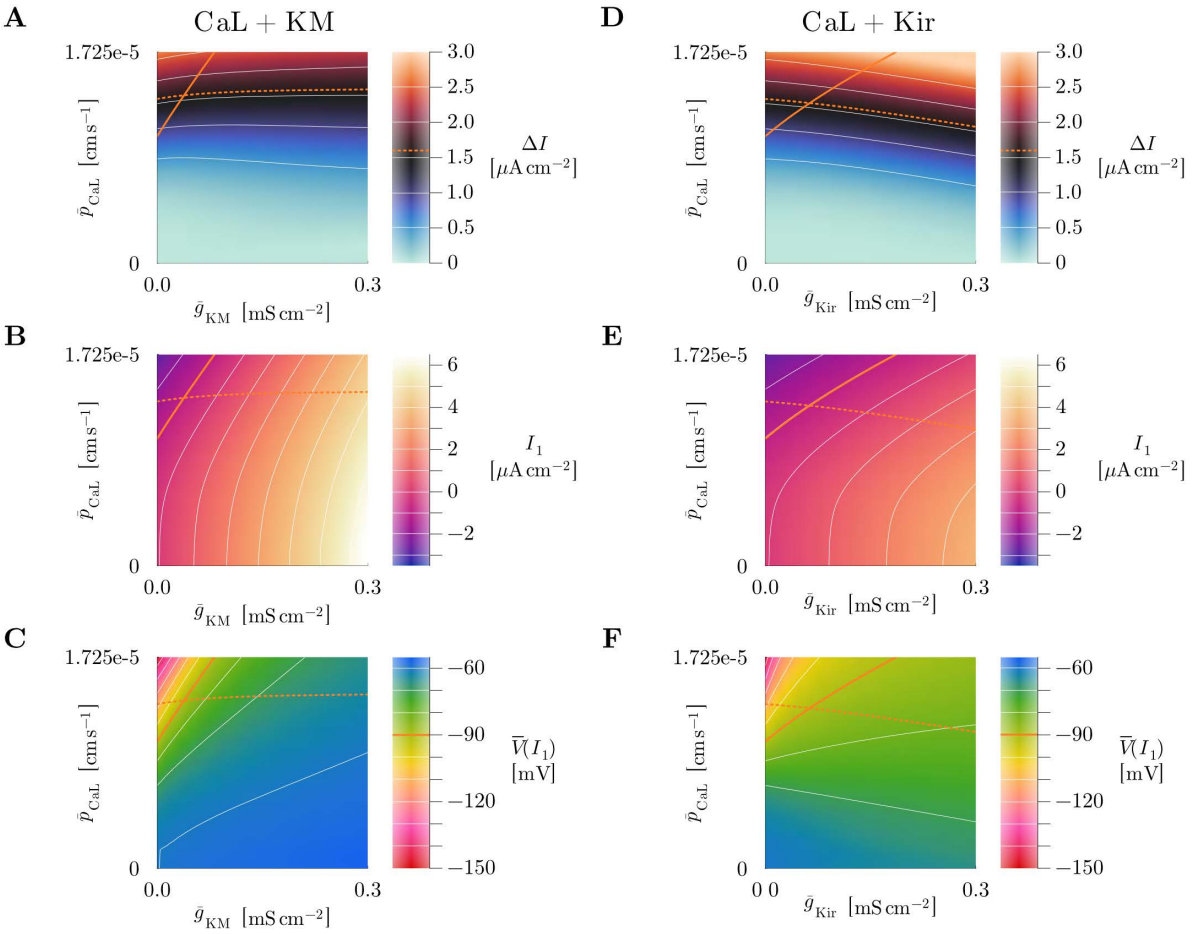

Fig 3. KM and Kir channels have distinct effects on the bistability window size, while both redress the resting equilibria. A–C: Heatmaps of the bistability window size $\Delta I = I_2 - I_1$ **(A)**, its lower limit I_1 **(B)**, and the corresponding resting equilibrium $\bar{V}(I_1)$ **(C)**, as a function of $\bar{p}_{\mathrm{CaL}}$ and $\bar{g}_{\mathrm{KM}}$. D–F: Same quantities as a function of $\bar{p}_{\mathrm{CaL}}$ and $\bar{g}_{\mathrm{Kir}}$. Each heatmap contains 51 × 47 data points ($\bar{g}_{\mathrm{KM}}$ and $\bar{g}_{\mathrm{Kir}}$ in steps of 0.006 mS/cm^2; $\bar{p}_{\mathrm{CaL}}$ in steps of 3.75×10^{-7} cm s^{-1}). White lines are contour lines. The red solid line marks $\bar{V}(I_1) = -90$ mV and the red dashed line marks $\Delta I = 1.6$ μA/cm^2. The two red lines together delimit the parameter region (top right) in which bistability is simultaneously robust ($\Delta I \geq 1.6$ μA/cm^2) and physiological ($\bar{V}(I_1) \geq -90$ mV).

https://doi.org/10.1371/journal.pcbi.1014549.g003

bistability window of $\Delta I_0 = 2.03$ μA/cm^2 (with $\bar{p}_{\mathrm{CaL}} = 1.5 \times 10^{-5}$ cm s^{-1}), we examined how co-varying $\bar{g}_{\mathrm{KM}}$ and $\bar{g}_{\mathrm{Kir}}$ (each from 0 to 0.3 mS/cm^2) affected ΔI (Fig 4A). Consistent with Fig 3A, increasing $\bar{g}_{\mathrm{KM}}$ reduced ΔI. For $\bar{g}_{\mathrm{KM}} \leq 0.15$ mS/cm^2, increasing $\bar{g}_{\mathrm{Kir}}$ monotonically increased ΔI, while for higher $\bar{g}_{\mathrm{KM}}$ values, a small reduction in ΔI (up to 0.11 μA/cm^2) was observed as $\bar{g}_{\mathrm{Kir}}$ increased. This local reduction likely reflects a transient phenomenon originating from higher-order interactions between the two conductances, as a similar drop (at most 0.05 μA/cm^2 was observed for $\bar{g}_{\mathrm{KM}}$ between 0.15 and 0.21 mS/cm^2 at low $\bar{g}_{\mathrm{Kir}}$, followed by a continuous increase in ΔI as $\bar{g}_{\mathrm{Kir}}$ increased. Thus, while the effect of $\bar{g}_{\mathrm{Kir}}$ on ΔI may become non-monotonic when combined with high $\bar{g}_{\mathrm{KM}}$, it generally acts to increase ΔI. $\bar{V}(I_1)$ rose more steeply with $\bar{g}_{\mathrm{KM}}$ than with $\bar{g}_{\mathrm{Kir}}$ (Fig 4B), confirming that Kir channels maintain resting equilibria in a lower voltage range than KM channels, even when combined. This is further illustrated in Fig 4C: at high $\bar{g}_{\mathrm{Kir}}$ and low $\bar{g}_{\mathrm{KM}}$, $\bar{V}(I)$ within the bistability window ranged from −82.6 to –64.6 mV (pink), whereas at low $\bar{g}_{\mathrm{Kir}}$ and high $\bar{g}_{\mathrm{KM}}$, it shifted to −64.6 to –56.4 mV with a smaller ΔI (purple). Increasing $\bar{g}_{\mathrm{Kir}}$ in the latter condition slightly lowered $\bar{V}(I)$ to −67 to –57.6 mV, despite a small reduction in ΔI of 0.08 μA/cm^2 (yellow). A similar analysis at half the baseline $\bar{p}_{\mathrm{CaL}}$ (see S3 Appendix) showed that while Kir and KM

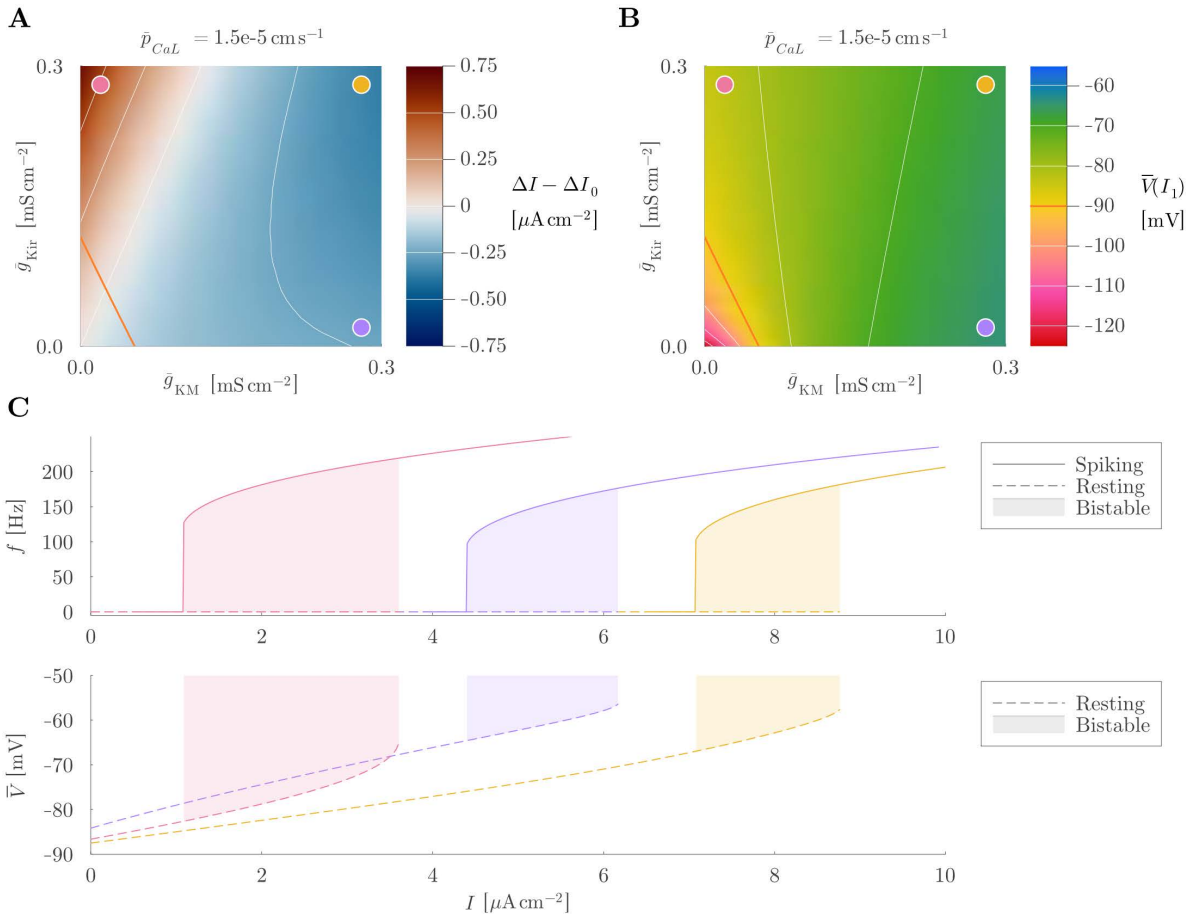

Fig 4. When combined, Kir and KM channels retain their individual effects on the bistability window. A: Heatmap of the change in bistability window size, $\Delta I - \Delta I_0$, as a function of $\bar{g}_{KM}$ and $\bar{g}_{Kir}$, with $\bar{p}_{CaL} = 1.5 \times 10^{-5}$ cm s^{-1} fixed. $\Delta I_0 = 2.03$ μA/cm^2 denotes the window size at $\bar{g}_{KM} = \bar{g}_{Kir} = 0$. B: Heatmap of $\overline{V}(I_1)$ over the same parameter grid. C: fI curves (top) and corresponding resting equilibria (bottom) for the three parameter sets marked in A and **B.** Each heatmap contains 31 × 31 data points. White lines are contour lines. The red solid line in A and B marks $\overline{V}(I_1) = -90$ mV.

https://doi.org/10.1371/journal.pcbi.1014549.g004

channels promote distinct ranges of resting equilibria, KM channels can slightly increase ΔI when ΔI is too small to be considered robust ($\Delta I_0 = 0.34 < 1.6$ μA/cm^2; largest increase: 0.14 μA/cm^2 at $\bar{g}_{Kir} = 0$). Altogether, the effects observed in isolation persisted when both channels were combined: Kir channels promote robust bistability by enlarging ΔI, whereas KM channels generally slightly reduce it.

The effects of CaL and Kir channels on bistability remain in the presence of additional conductances

To test whether these effects generalize beyond the minimal model, we repeated the analysis on a published two-compartment model of deep projection neurons that already includes CaL channels in the dendrite and Kir channels in the soma, alongside calcium-dependent potassium (KCa) channels in both compartments, calcium-dependent nonspecific cation (CAN) channels in the dendrite, and a faster L-type calcium current (CaL, f) in the soma [29]. We varied only $\bar{p}_{CaL}$ and $\bar{g}_{Kir}$ and kept the other conductances at their published values.

We first examined the response of four illustrative pairs ($\bar{p}_{CaL}, \bar{g}_{Kir}$) to pulses of current of either 50 or 150 pA, each with a baseline current producing a resting equilibrium of –65 mV. At low values of both conductances ($\bar{p}_{CaL} = 2 \times 10^{-6}$ cm s^{-1}

and $\bar{g}_{Kir}$ = 0.015 mS/cm^2), no bistability was observed (Fig 5A). Raising $\bar{g}_{Kir}$ alone to 0.185 mS/cm^2 (Fig 5B), $\bar{p}_{CaL}$ alone to 1.5×10^{-5} cm s^{-1} (Fig 5C), or both together (Fig 5D) all produced bistability. The fI curves resulting from the first and the second pairs of conductances (used in Fig 5A and 5B, respectively), each with $\bar{p}_{CaL} = 2 \times 10^{-6}$ cm s^{-1}, did not display a significant bistability window, as only the second pair of conductance exhibited a small ΔI of 6.3 pA (Fig 5E, top). Increasing $\bar{g}_{Kir}$ hyperpolarized $\overline{V}(I_2)$ from −47 to –63 mV and increased I_1 (Fig 5E, bottom). With $\bar{p}_{CaL}$ raised to 1.5×10^{-5} cm s^{-1}, ΔI increased to 133 pA and 151.1 pA for $\bar{g}_{Kir}$ = 0.015 and 0.185 mS/cm^2, respectively, while increasing $\bar{g}_{Kir}$ again hyperpolarized $\overline{V}(I_2)$ from −48 to –63 mV and increased I_1 (Fig 5F). The difference in pulse amplitude across Fig 5A–5D

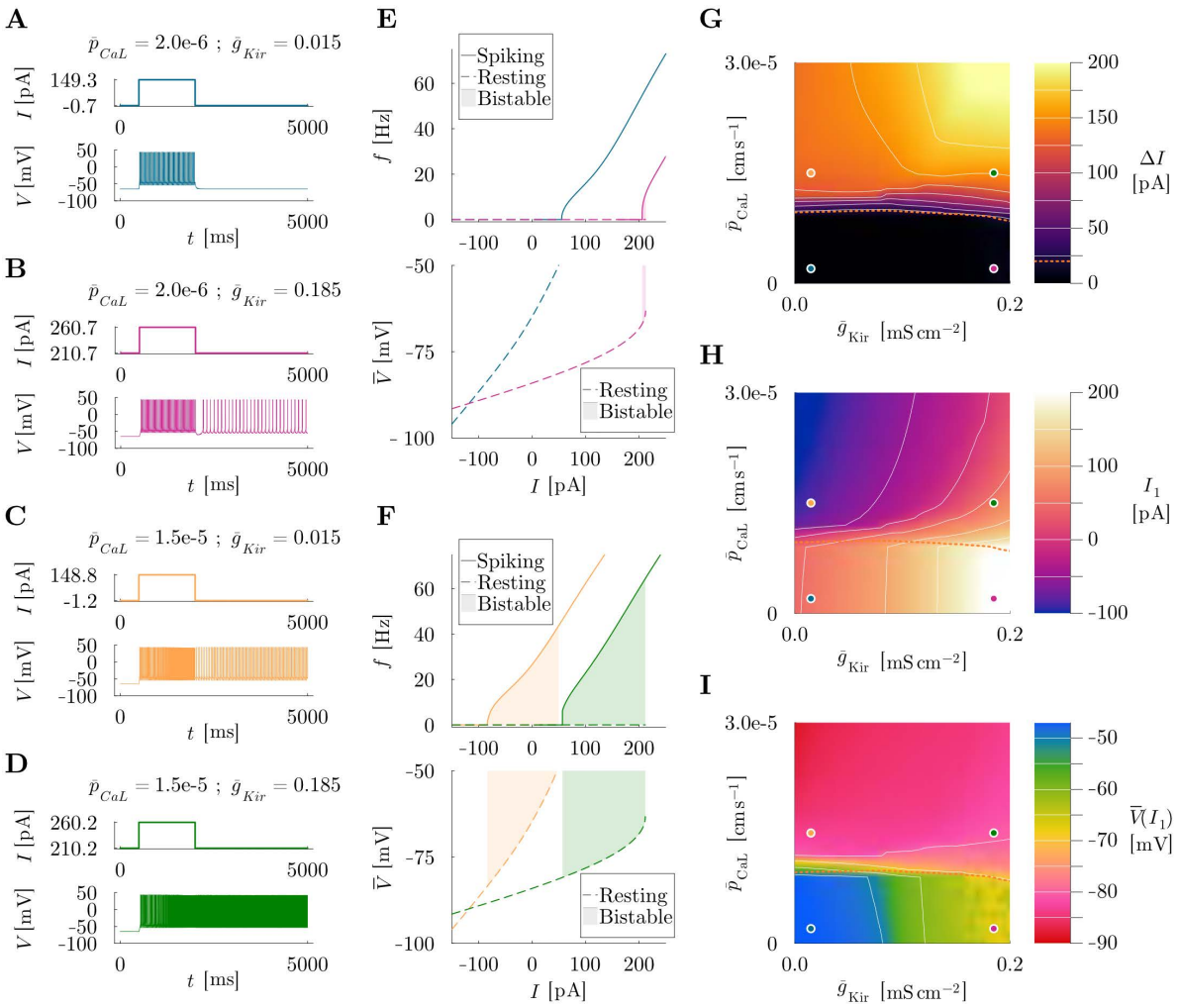

Fig 5. In a two-compartment model of deep projection neurons including additional ion channels, CaL and Kir channels retain their effects on bistability. A: Response of the model with low $\bar{p}_{CaL} = 2 \times 10^{-6}$ cm s^{-1} and low $\bar{g}_{Kir}$ = 0.015 mS/cm^2, initially at –65 mV, to a 150 pA current pulse. B: Same as A with $\bar{g}_{Kir}$ raised to 0.185 mS/cm^2 and a 50 pA pulse. C: Same as A with $\bar{p}_{CaL}$ raised to 1.5×10^{-5} cm s^{-1}. D: Same as C with $\bar{g}_{Kir}$ also raised to 0.185 mS/cm^2 and a 50 pA pulse. E: fI curves (top) and corresponding resting equilibria (bottom) for the parameter sets used in A and C, isolating the effect of raising $\bar{p}_{CaL}$. F: Same as E for the parameter sets used in B and **D.** G–I: Heatmaps of the bistability window size ΔI **(G)**, its lower limit I_1 **(H)**, and the corresponding resting equilibrium $\overline{V}(I_1)$ **(I)**, as a function of $\bar{p}_{CaL}$ and $\bar{g}_{Kir}$. Each heatmap contains 41 × 31 data points. White lines are contour lines. The red dashed line marks ΔI = 20 pA, the robustness threshold estimated from published experimental data of afterdischarges. All parameter combinations shown in G–I satisfy $\overline{V}(I_1) \geq$ –90 mV, so robust and physiological bistability coincides with the region above the red dashed line.

https://doi.org/10.1371/journal.pcbi.1014549.g005

(50 vs 150 pA) reflects the fact that, at high $\bar{g}_{Kir}$, a current of only 10 pA was sufficient to cross I_1 from a resting equilibrium of –65 mV.

A systematic sweep over the two conductances reproduced the minimal model pattern (Fig 5G): ΔI grew with $\bar{p}_{CaL}$, and, for $\bar{p}_{CaL}$ between 1.5×10^{-5} and 3×10^{-5} cm s^{-1}, also with $\bar{g}_{Kir}$. The increase in ΔI with $\bar{p}_{CaL}$ appeared to saturate for $\bar{g}_{Kir} \leq 0.1$ mS/cm^2. Doubling $\bar{p}_{CaL}$ from 1.5×10^{-5} to 3×10^{-5} cm s^{-1} increased ΔI by only 4 pA at $\bar{g}_{Kir}$ = 0 and 21 pA at $\bar{g}_{Kir}$ = 0.1 mS/cm^2. Above this value, ΔI became more sensitive to $\bar{p}_{CaL}$, reaching an increase of 55 pA at $\bar{g}_{Kir}$ = 0.2 mS/cm^2. At lower $\bar{p}_{CaL}$ (between 1×10^{-5} and 1.5×10^{-5} cm s^{-1}), ΔI still increased overall with $\bar{g}_{Kir}$, but exhibited a transient drop of up to 25 % relative to its value at $\bar{g}_{Kir}$ = 0 before rising again.

I_1 and $\overline{V}(I_1)$ followed the same patterns as in the minimal model (Fig 5H–5I). Raising $\bar{p}_{CaL}$ lowered I_1 and hyperpolarized $\overline{V}(I_1)$, while raising $\bar{g}_{Kir}$ raised I_1. The effect of $\bar{g}_{Kir}$ on $\overline{V}(I_1)$ depended on whether bistability was already established. With a well-developed bistability window ($\bar{p}_{CaL}$ between 1.5×10^{-5} and 3×10^{-5} cm s^{-1}), increasing $\bar{g}_{Kir}$ depolarized $\overline{V}(I_1)$ by up to 5 mV. Where bistability was weak or absent ($\bar{p}_{CaL} < 1 \times 10^{-5}$ cm s^{-1}, $\Delta I < 30$ pA), it hyperpolarized $\overline{V}(I_1)$ by up to 25 mV. At intermediate $\bar{p}_{CaL}$ values, the effect transitioned from hyperpolarization to depolarization as bistability emerged.

These results confirm that the minimal model findings generalize to a more realistic setting: CaL channels create bistability, Kir channels enlarge the window, and both effects persist in the presence of KCa, CAN, and CaL, f currents. Accounting for the soma surface area (1×10^{-4} cm^2), a 200 pA window in the two-compartment model corresponds to 2 μA/cm^2 in the minimal model. Although KM channels were not originally included in the two-compartment model, replacing Kir channels with KM channels in a full parameter sweep reduced ΔI, consistent with the minimal model results, and in some cases eliminated bistability altogether (see S4 Appendix). Having established that the effects generalize, we next ask whether the two pairs also differ in their robustness to noise and intrinsic variability.

Bistability is more robust to noisy inputs and intrinsic variability when CaL and Kir channels are combined

We next asked whether the bistabilities produced by CaL + KM and CaL + Kir pairs differ in robustness to noisy inputs and to intrinsic variability. To compare the two pairs on equal footing, we selected a CaL + KM set and a CaL + Kir set with matching bistability window sizes; because KM channels reduce ΔI while Kir channels enlarge it, this required a higher $\bar{p}_{CaL}$ for the CaL + KM pair, while $\bar{g}_{KM}$ and $\bar{g}_{Kir}$ were set to the same value.

With CaL + KM channels, the resting state was lost under small perturbations while spiking was maintained up to the largest noise levels tested. Applying the central current of the bistability window with superimposed white noise of increasing standard deviation σ, the initially resting neuron transitioned to spiking within the first few tens of seconds (Fig 6A), whereas the initially spiking neuron kept spiking (Fig 6B). Across 500 trials at each fixed σ, the proportion of resting-to-spiking transitions grew rapidly with σ, while spiking-to-resting transitions never occurred in our range (Fig 6C).

With CaL + Kir channels, both states could be lost under sufficient noise, and the two states were of comparable robustness. The initially resting neuron transitioned to spiking at moderate σ (Fig 6D), and the initially spiking neuron transitioned to resting at slightly higher σ, with each resting episode lasting a few hundred milliseconds before spiking resumed (Fig 6E). Spiking was more robust than resting in $\bar{g}$Kir-bistability, tolerating higher noise levels even when kept constant over time (Fig 6F), in contrast to $\bar{g}$KM-bistability where resting was highly fragile while spiking remained undisrupted (Fig 6C).

This asymmetry in robustness raises the question of whether both states are equally reachable, particularly in $\bar{g}_{KM}$-bistability where resting may be almost unreachable. To address this, we simulated the neuron response to a constant current within the bistability window (i.e., between I_1 and I_2) in noise-free conditions, for both $\bar{g}_{Kir}$ and $\bar{g}_{KM}$-bistability, starting from initial conditions

$$(V_0, m_{ion,\infty}(V_0), h_{ion,\infty}(V_0), \ldots, \left[Ca^{2+}\right]_0) \text{ with } V_0 \in [-90, -20] \text{ mV},$$

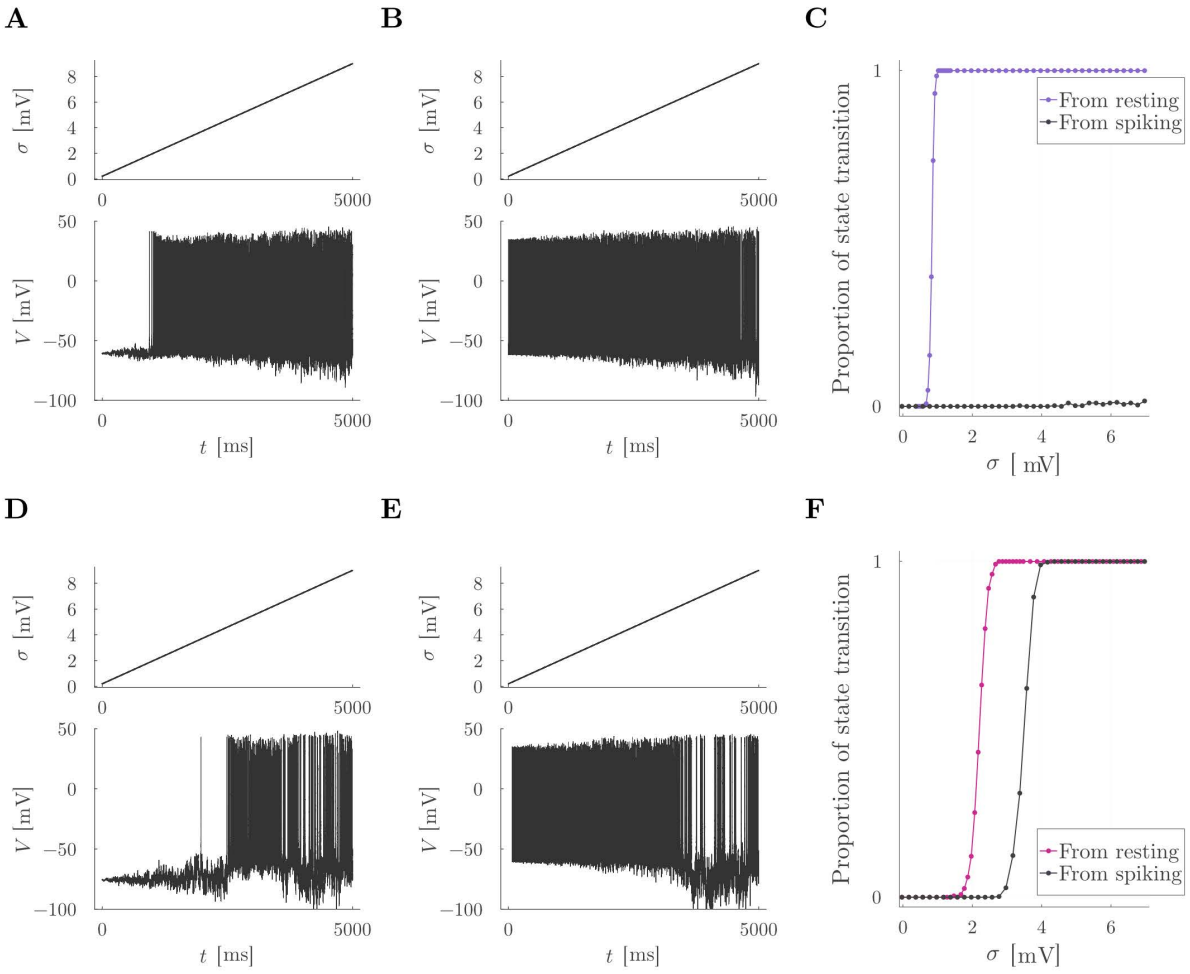

Fig 6. Resting and spiking show different robustness to noise depending on whether KM or Kir channels are combined with CaL channels. A: Membrane potential of the CaL + KM model in response to the central current of the bistability window, with superimposed white noise of increasing standard deviation σ, starting from the resting state. B: Same as A, starting from the spiking state. C: Proportion of 500 trials that transitioned away from the initial state (resting→spiking or spiking→resting) as a function of σ held constant throughout each trial, for the CaL + KM model. D–F: Same as A–C for the CaL + Kir model. The two models were matched for bistability window size: $\bar{g}_{KM}$ (A–C) and $\bar{g}_{Kir}$ (D–F) were set to the same value, while $\bar{p}_{CaL}$ was higher in the CaL + KM model to compensate for the narrowing effect of KM channels.

https://doi.org/10.1371/journal.pcbi.1014549.g006

and recorded the state to which the model converged (Fig 7). With CaL + Kir channels (Fig 7A), resting was more reachable than with CaL + KM channels (Fig 7B), the latter showing lower reachability of resting throughout the bistability window, while spiking showed the opposite trend. These results were consistent with those in Fig 6, obtained at the center of each bistability window. Near I_2, the contrast was particularly striking: in $\bar{g}_{KM}$-bistability, only initial conditions close to $\overline{V}(I_2)$ converged to resting, making this state extremely difficult to reach and maintain. These results also showed that state reachability varied within each bistability window, suggesting that noise robustness should similarly depend on the applied current. Consistently, repeating the experiment of Fig 6 at $I = I_1$ instead of $(I_1 + I_2)/2$ showed that resting became more robust than spiking in both bistability types, while resting in $\bar{g}_{Kir}$-bistability remained more robust than in $\bar{g}_{KM}$-bistability (see S5 Appendix).

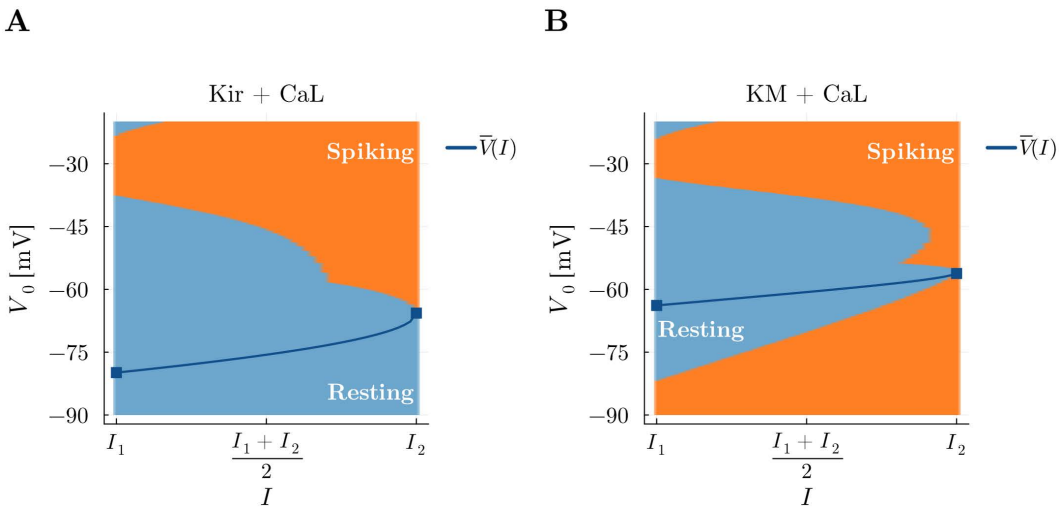

Fig 7. The reachability of resting and spiking across the bistability window depends on which potassium channel is combined with CaL. A: Final state reached by the CaL + Kir model as a function of the applied current (within $[I_1, I_2]$) and the initial membrane potential $V_0 \in [-90, -20]$ mV. Blue indicates convergence to resting, orange to spiking. The dark blue line traces $\bar{V}(I)$ within the bistability window. B: Same as A for the CaL + KM model.

https://doi.org/10.1371/journal.pcbi.1014549.g007

We next investigated how both bistability types responded to intrinsic variability, estimating how ΔI evolved across heterogeneous neurons. The membrane capacitance (C), maximal sodium conductance ($\bar{g}_{Na}$), and leak conductance (g_{leak}) were each sampled uniformly within ±10%, ±20%, or ±30% of their nominal values. The same conductance values were used for both bistability types ($\bar{g}_{Kir} = \bar{g}_{KM} = 0.3$ mS/cm^2, $\bar{p}_{CaL} = 1.5 \times 10^{-5}$ cm s^{-1}), yielding different ΔI. The resulting relative changes in ΔI were computed and represented as a function of C for each variability level (Fig 8A). Changes in C had opposite effects on the two bistability types, but with smaller magnitude for $\bar{g}_{Kir}$-bistability. At every level of intrinsic variability tested, relative changes in $\bar{g}_{KM}$-bistability were approximately 1.5 times larger than in $\bar{g}_{Kir}$-bistability, which remained within ±20% (Fig 8B).

Ion channels increasing bistability have a steady-state current exhibiting a region of negative differential conductance

The opposing effects of KM and Kir channels on ΔI must arise from the shapes of their steady-state currents, since both are voltage-gated potassium channels operating on a similar timescale. We therefore compared the steady-state currents of CaL, KM, and Kir channels, focusing on their differential conductance around the spike threshold (≈ -65 mV).

CaL channels carry an inward current (Fig 9A, top) with a region of negative differential conductance near the spike threshold (Fig 9A, shaded area). Previous work has linked this feature to the onset of bistability [13,30]: a small depolarization within this range increases the inward calcium current, which depolarizes the membrane further and triggers spiking at a lower applied current, thereby reducing I_1. Because CaL channels barely affect the values of resting equilibria (see Fig 1C and S1 Appendix prior to the addition of CaL channels), resting at a smaller I_1 must be balanced by a stronger leak current, that dominates the sum of ionic currents below –60.1 mV (the reversal potential of the leak current). This accounts for the hyperpolarization of $\bar{V}(I_1)$ observed in Figs 1C and 3C.

Unlike CaL channels, KM channels carry a small inward and a strong outward current (Fig 9B, top), both with strictly positive differential conductance (Fig 9B, bottom). Empirically, increasing $\bar{g}_{KM}$ shifts both I_1 and I_2 upward, but raises I_1 more than I_2, thereby reducing ΔI (Figs 1C and 2B–2C). This asymmetric shift follows from I_1 and I_2 being governed by different dynamical states: spiking at I_1 and resting at I_2. When initially spiking at I_1, the membrane potential is overall

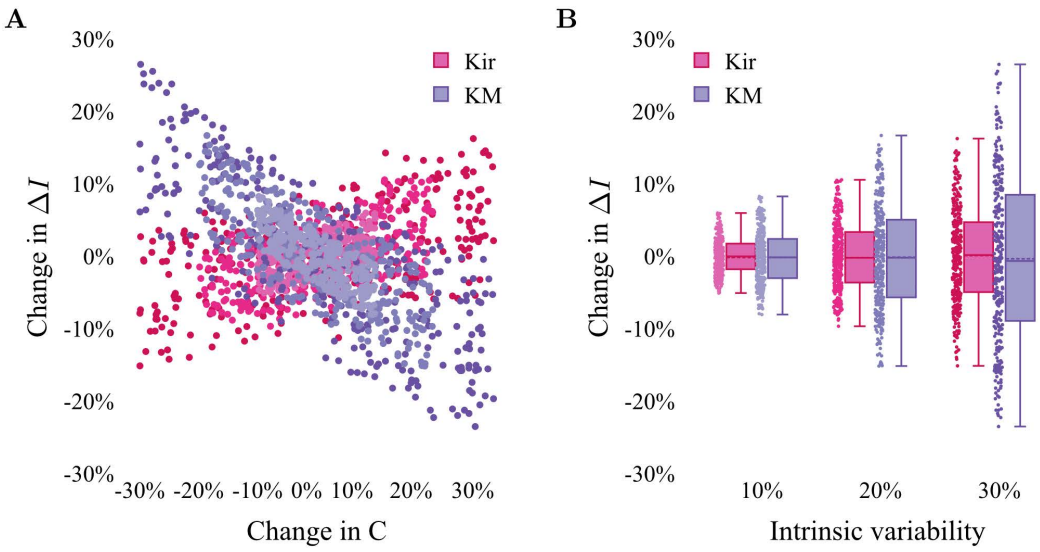

Fig 8. Intrinsic variability affects the bistability window size more strongly in CaL + KM than in CaL + Kir bistability. A: Relative change in bistability window size (ΔI) as a function of the sampled membrane capacitance C, for the CaL + Kir (pink) and CaL + KM (purple) models. Shades of each color correspond to variability levels of ±10%, ±20%, and ±30% applied simultaneously to C, the sodium maximal conductance, and the leak conductance. B: Boxplots of the relative changes in ΔI at each variability level, for the two models.

https://doi.org/10.1371/journal.pcbi.1014549.g008

higher than the resting equilibrium at I_2. Since KM channels have positive differential conductance, they produce a stronger outward current in the spiking scenario at I_1 than in the resting scenario at I_2, requiring a larger compensating current increase at I_1. Additionally, increasing $\bar{g}_{KM}$ elevates $\overline{V}(I)$ (Fig 2C), as KM channels provide a non-negligible current at these potentials and, together with the leak current, dominate the sum of ionic currents at rest, causing $\overline{V}(I_1)$ and $\overline{V}(I_2)$ to rise with I_1 and I_2 (Fig 3C). For a fixed applied current (e.g., I = –0.1 μA/cm^2), KM channels hyperpolarize the resting equilibrium toward E_K (from $\overline{V}$ = –60.9 mV in Fig 1C to below –75 mV in Fig 2C).

In contrast to KM channels, Kir channels carry a strong inward current below E_K and a weaker outward current (Fig 9C, top), and share with CaL channels a region of negative differential conductance around the spike threshold (Fig 9C, bottom). By analogy with the CaL current, this negative-slope region promotes the resting-to-spiking transition: a small depolarization decreases the outward Kir current, which depolarizes the membrane further. Like KM channels, increasing $\bar{g}_{Kir}$ shifts both I_1 and I_2 upward, but the shift is larger for I_2 than for I_1, in contrast to KM channels, thereby increasing ΔI (Figs 1C and 2E–2F). By the same reasoning as for KM channels, Kir channels produce a lower outward current in the spiking scenario at I_1 than in the resting scenario at I_2, requiring a larger compensating current increase at I_2 because of the negative differential conductance of the outward Kir current. Increasing $\bar{g}_{Kir}$ generally elevates $\overline{V}(I)$ (Fig 2F), as Kir channels dominate the sum of ionic currents at rest, though their effect is non-linear. Below –67 mV, Kir channels display positive differential conductance, which steepens the sum of ionic currents at rest. In this region, the rise in I_1 induced by increasing $\bar{g}_{Kir}$ therefore depolarizes $\overline{V}(I_1)$ (Figs 2F and 3F, upper half). Above –67 mV, the Kir current increasingly dominates the sum of ionic currents as the potential approaches –60.1 mV, since the leak current diminishes near its reversal potential. In this region, however, the Kir current displays negative differential conductance, creating a negative-slope region in the sum of ionic currents near –60.1 mV. To understand the contribution of Kir channels to $\overline{V}(I_2)$, consider a neuron with the same conductances as in Fig 2F, initially resting at I_1, with the applied current progressively increased. As the membrane potential rises, the positive differential conductance of the Kir current initially allows the sum of ionic currents to compensate for the depolarization. This compensation reaches its limit at $\delta(\Sigma I_{ion})/\delta V = 0$, just before the negative-slope region of the sum of ionic currents, determining $\overline{V}(I_2)$. As $\bar{g}_{Kir}$ increases, the negative-slope region grows, shifting this limit to more

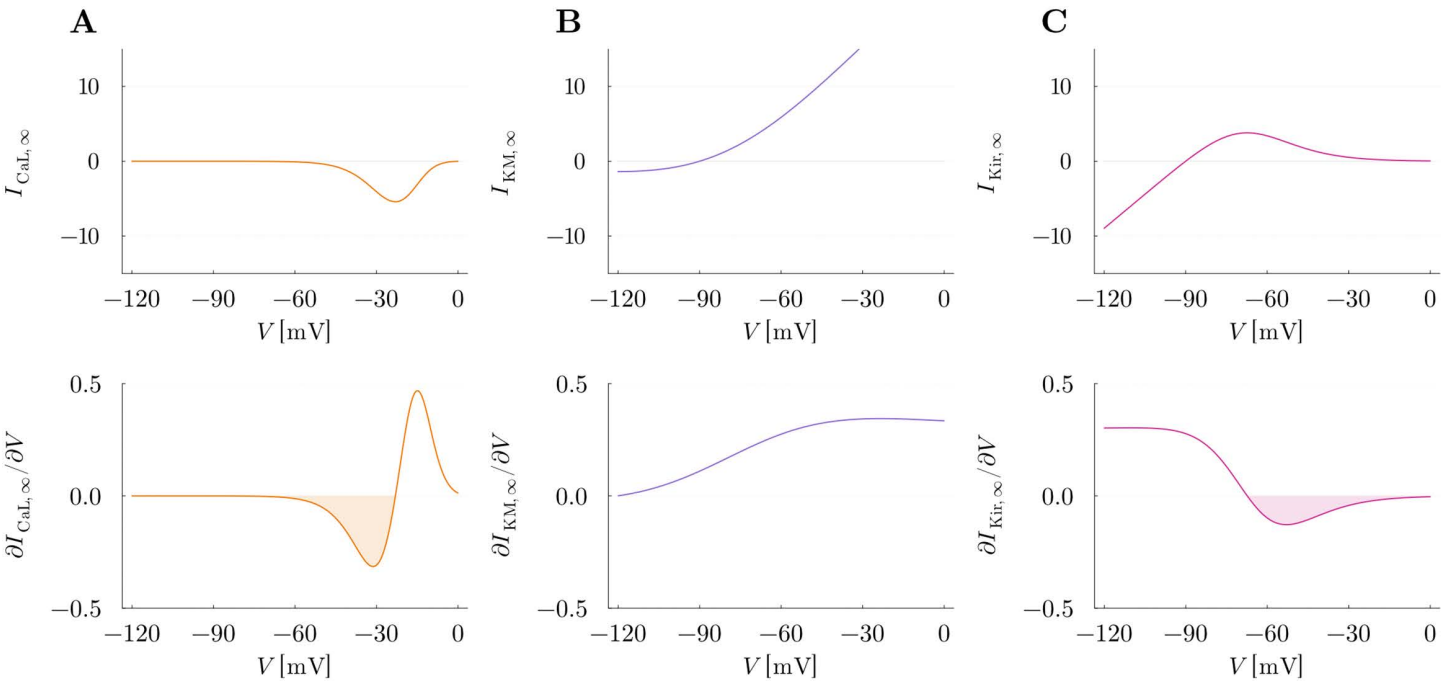

Fig 9. Steady-state currents of CaL, KM, and Kir channels and their differential conductance. A: Steady-state L-type calcium current $I_{\mathrm{CaL},\infty}$ (top) and its differential conductance (bottom), at an intracellular calcium concentration of 2 mM. The region of negative differential conductance around the spike threshold is shaded. B: Same as A for the KM current $I_{\mathrm{KM},\infty}$, which has positive differential conductance throughout. C: Same as A for the Kir current $I_{\mathrm{Kir},\infty}$, which has a region of negative differential conductance above E_{K} (shaded). The y-scale of the steady-state currents is in μA/cm² (top) and that of the differential conductance in μA/mV cm². A,B,C used respectively $\bar{p}_{\mathrm{CaL}} = 1.5 \times 10^{-5}$ cm s^{-1}, $\bar{g}_{\mathrm{KM}} = 0.3$ mS/cm², and $\bar{g}_{\mathrm{Kir}} = 0.3$ mS/cm².

https://doi.org/10.1371/journal.pcbi.1014549.g009

hyperpolarized potentials and thus progressively hyperpolarizing $\overline{V}(I_2)$, as observed when $I_2 = I_1$ for $\Delta I = 0$ and $\bar{p}_{\mathrm{CaL}} \sim 0$ in Fig 3F.

Both KM and Kir channels produce an asymmetric shift in I_1 and I_2, which respectively narrows or enlarges ΔI. This asymmetry arises because I_1 and I_2 are set by the appearance and disappearance of two different behaviors, governed by distinct dynamical mechanisms that rely on different types of bifurcations (examined later, Fig 11). These mechanisms are potentially shaped by the sign of the differential conductance around the spike threshold, suggesting that its sign predicts whether a potassium channel enlarges or narrows ΔI. We test this hypothesis in the next subsection by selectively blocking the inward and outward components of each current.

The inward currents redress resting equilibria and maintain bistability, but the outward potassium currents either increase or decrease bistability

If the sign of the differential conductance around the spike threshold dictates the effect on ΔI, then only the outward component of each potassium current, which carries that differential conductance, should reshape the bistability window, while the inward component, being zero above E_{K}, should not interfere with spiking. We tested this by blocking either the inward or the outward component of each current in turn, measuring the resulting ΔI and the resting equilibria $\overline{V}(I)$ within the bistability window, the latter being determined by applying hyperpolarizing current steps between I_1 and I_2.

To isolate the inward KM current, the outward component was blocked above E_{K} (Fig 10A, left). With only its inward component active, the KM current did not alter ΔI (Fig 10A, center). Hyperpolarizing steps within the bistability window showed that it only slightly raised the resting equilibria that lay below E_{K} (Fig 10A, right). Conversely, isolating the outward

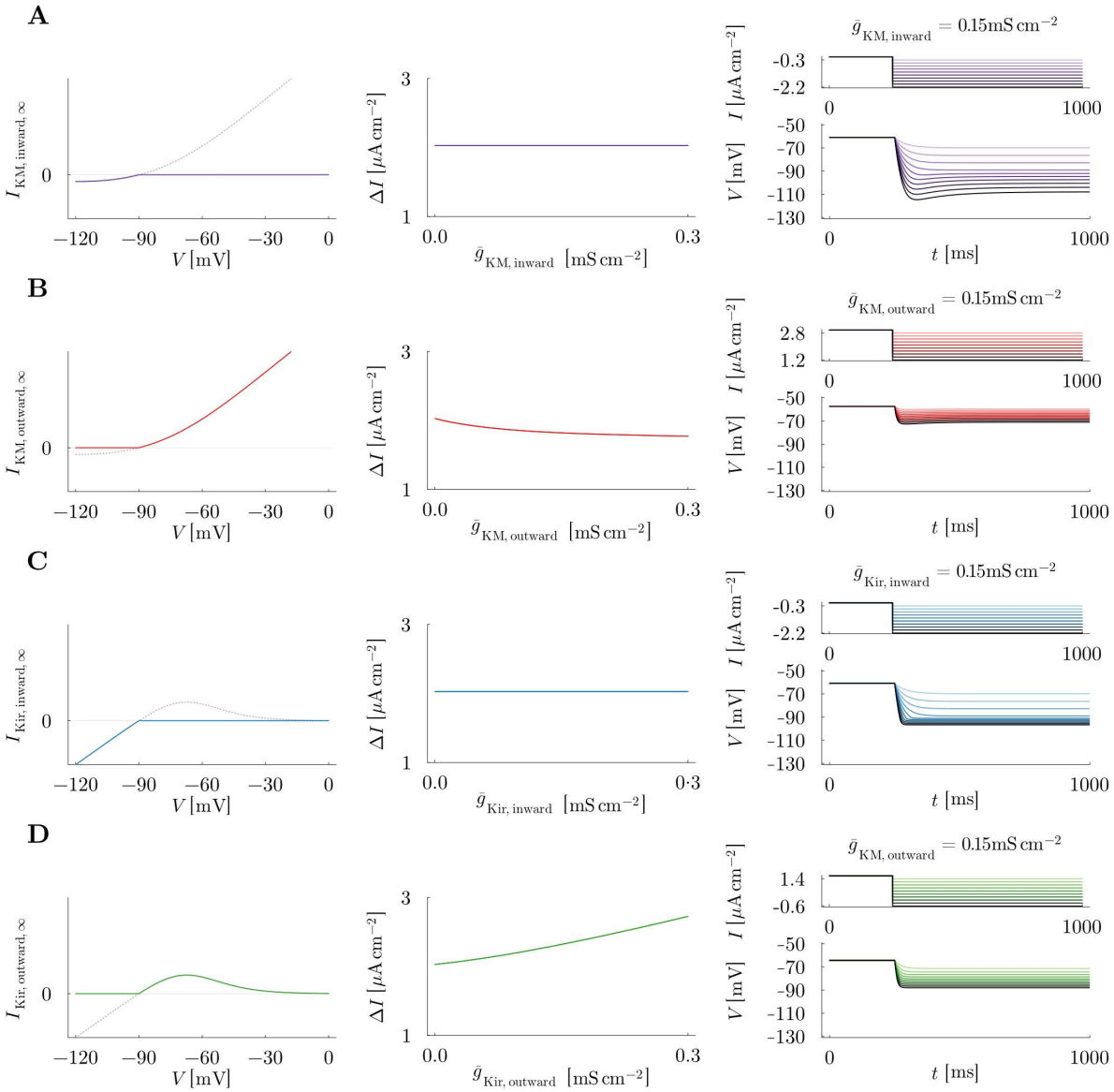

Fig 10. Inward components of both currents redress resting equilibria below –90 mV, while outward components reshape the bistability window in opposite directions. A: Steady-state KM current with the outward component blocked (left), bistability window size ΔI as a function of the inward conductance $\bar{g}_{\mathrm{KM,inward}}$ (center), and hyperpolarizing steps of current across the window at a fixed $\bar{g}_{\mathrm{KM,inward}}$ (right). B: Same as A with the inward component of the KM current blocked instead. C: Same as A for the Kir current, with the outward component blocked. D: Same as A for the Kir current, with the inward component blocked. In the right-hand panels, the maximum and minimum applied currents equal I_1 and I_2 for each blocked condition, at a conductance of 0.15 mS/cm^2.

https://doi.org/10.1371/journal.pcbi.1014549.g010

KM current by blocking the inward component (Fig 10B, left) showed that increasing $\bar{g}_{\mathrm{KM,outward}}$ narrowed ΔI while efficiently adjusting resting equilibria (Fig 10B, center–right).

Blocking the outward Kir current isolated the inward component (zero above E_{K}, Fig 10C, left), which left ΔI unchanged as $\bar{g}_{\mathrm{Kir,inward}}$ increased (Fig 10C, center), but efficiently hyperpolarized resting equilibria up to E_{K} (Fig 10C, right). This correction was more efficient than for the inward KM current, due to the larger amplitude of the inward Kir

current. Conversely, blocking the inward Kir current isolated the outward component (non-zero above E_K, Fig 10D, left), which enlarged the bistability window as $\bar{g}_{Kir,outward}$ increased, while only adjusting resting equilibria above E_K (Fig 10D, center–right).

These four experiments together show a clear partition of roles. The inward components of both KM and Kir currents act only on resting equilibria below E_K and leave ΔI unchanged, since the spike threshold lies above E_K and the inward currents vanish there. The outward components redress the remaining resting equilibria and, in addition, act on ΔI: the outward KM current narrows it while the outward Kir current enlarges it. This difference is consistent with the sign of their differential conductance around the spike threshold, which is positive for KM and negative for Kir, confirming the hypothesis of the previous subsection.

CaL and Kir channels facilitate the generation of plateau potentials, whereas KM channels induce a distinct excitability switch

The qualitative changes in $\overline{V}(I_1)$ and ΔI observed as $\bar{p}_{CaL}$, $\bar{g}_{Kir}$, or $\bar{g}_{KM}$ increases (Fig 3) suggest that each channel type triggers a distinct excitability switch, that is, a qualitative change in how the neuron approaches or leaves the spiking regime. To identify these switches, we used the minimal conductance-based model containing only I_{Na}, I_{KDR}, and I_{leak} as a reference, and compared it to three variants in which CaL, Kir, or KM channels were added individually. For each condition we recorded the response to a hyperpolarizing current step crossing I_1 (Fig 11 A–11D) and computed the bifurcation diagram of the membrane potential as a function of the applied current (Fig 11 E–11H).

In the reference condition ($\bar{p}_{CaL} = \bar{g}_{Kir} = \bar{g}_{KM} = 0$), reducing the applied current below I_1 causes the neuron to settle directly to a resting equilibrium within the range of potentials spanned by spiking (Fig 11 A). The bifurcation diagram confirmed this, showing that resting equilibria near I_1 exceeded the minimum of the spiking limit cycle (Fig 11 E). The overlap between I_1 and I_2 reflects the absence of bistability, as spiking appeared precisely when resting disappeared. As the applied current increased, the resting state disappeared at I_2 through a saddle-node (SN) bifurcation, where the stable equilibrium collided with a saddle point. Since the stable equilibrium at I_2 lay within the spiking voltage range and spiking frequency near I_1 was of the order of a few hertz (Fig 11 A), the SN bifurcation occurred on an invariant circle, giving rise to a saddle-node on invariant circle (SNIC) bifurcation. By nature, the SNIC bifurcation is associated with low-frequency spiking at onset [31].

Adding CaL channels alone ($\bar{p}_{CaL} = 7.5 \times 10^{-6}$ cm s^{-1}) rendered the neuron bistable, and produced a plateau upon hyperpolarization below I_1 (Fig 11 B). This plateau represented a clear separation between the range of potentials encompassed by spiking and the resting equilibria below I_1, that are typically below the range of potentials covered by spiking. Bistability arose because the addition of CaL transformed the SNIC bifurcation into a separate SN bifurcation at I_2 and a saddle-homoclinic (SH) bifurcation at I_1 (Fig 11 F). The saddle-homoclinic bifurcation is defined by the collision between a saddle point and a homoclinic loop, which is defined by the high-dimensional model trajectory during spiking, at I_1, where spiking appears (for more details see [31]). However, the bifurcation diagram also revealed that the separation between resting equilibria and the spiking voltage range exists only near I_1, so the plateau observed upon hyperpolarization may not persist for currents closer to I_2 (Fig 11 F).

Adding Kir channels alone ($\bar{g}_{Kir} = 0.3$ mS/cm^2) produced a smaller plateau (Fig 11 C) but generated the same qualitative bifurcation structure as CaL channels, transforming the SNIC bifurcation into a separate SN bifurcation and a SH bifurcation (Fig 11 G). This shared bifurcation structure likely underlies the enlarging effect of Kir channels on ΔI. Notably, the voltage separation between resting equilibria and the spiking voltage range persisted throughout the entire bistability window, up to $I_2 = I_1$ (Fig 11 G).

Adding KM channels alone ($\bar{g}_{KM} = 0.3$ mS/cm^2) produces a qualitatively different switch. Instead of a plateau, the hyperpolarizing step elicits damped subthreshold oscillations as the neuron approaches a higher resting equilibrium (Fig 11 D). The bifurcation diagram revealed that the resting equilibria largely overlapped the spiking voltage range (Fig 11 H).

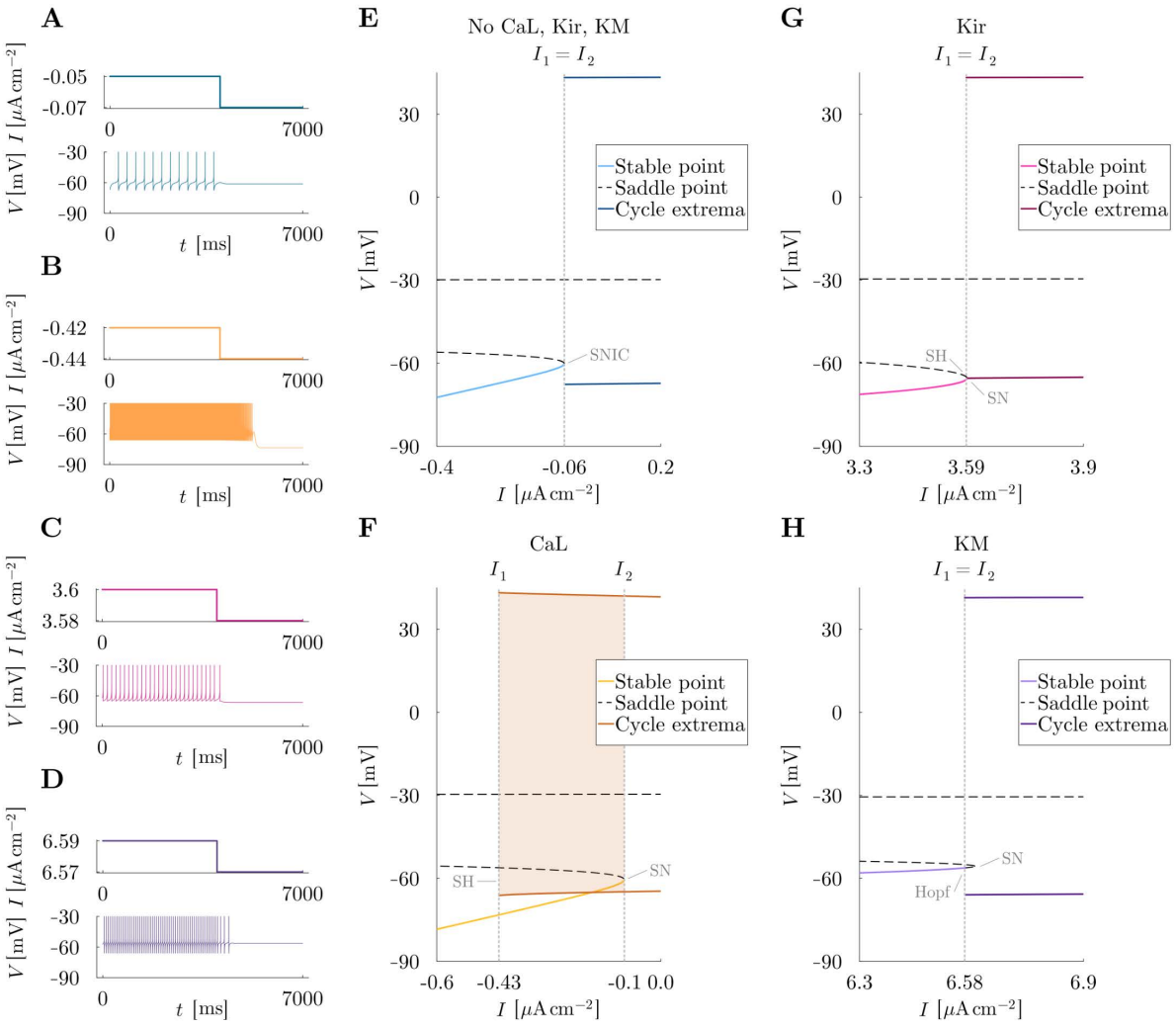

Fig 11. Excitability switches created by CaL, Kir, and KM channels, identified through bifurcation analysis. A–D: Response of the model to a hyperpolarizing current step crossing I_1, for four conditions. A: reference model (I_{Na}, I_{KDR}, I_{leak}). B: reference model + CaL channels. C: reference model + Kir channels. D: reference model + KM channels. In each panel the lower and upper current values are $I_1 \pm 10$ nA/cm^2 for the corresponding conductances. E–H: Bifurcation diagrams for the four conditions. Bifurcation types are labelled directly on each panel: SNIC (saddle-node on invariant circle), SN (saddle-node), SH (saddle-homoclinic), and Hopf.

https://doi.org/10.1371/journal.pcbi.1014549.g011

The resting state disappeared through a Hopf bifurcation rather than a SN bifurcation, as the stable equilibrium lost stability before colliding with the saddle point. The Hopf bifurcation confers resonator behavior, whereby the neuron preferentially responds to inputs at the resonant frequency of its subthreshold oscillations, in contrast to integrators associated with SN or SNIC bifurcations, which perform temporal integration of input pulses [32]. Intuitively, this lack of voltage separation means that a neuron transitioning from spiking to rest remains within the voltage range visited during spiking, making the resting state far easier to escape than in the SN + SH case, where the transition requires crossing a voltage region not visited during spiking.

When CaL and Kir channels are combined, the hyperpolarizing step produces a pronounced plateau (Fig 12A), and the bifurcation diagram preserves the SN + SH structure observed for each channel alone (Fig 12C). In contrast, combining CaL with KM channels suppresses the plateau (Fig 12B), as resting equilibria are pulled into the spiking voltage range

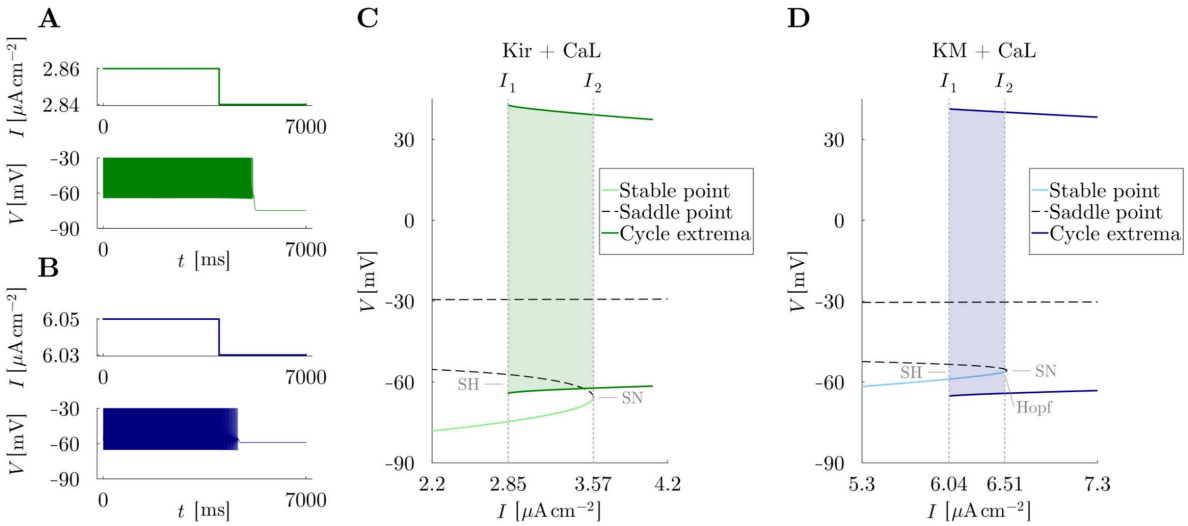

Fig 12. Combining CaL with Kir channels reinforces plateau potentials while combining CaL with KM channels suppresses them. A: Response of the CaL + Kir model to a hyperpolarizing current step crossing I_1. B: Same as A for the CaL + KM model. In A and B the lower and upper current values are $I_1 \pm 10$ nA/cm^2 for the corresponding conductances. The brief spiking following the step in B is an afterdischarge, not a plateau potential. C: Bifurcation diagram of the CaL + Kir model as a function of the applied current. D: Same as C for the CaL + KM model. Bifurcation types are annotated directly on the panel.

https://doi.org/10.1371/journal.pcbi.1014549.g012

and disappear at I_2 through a Hopf bifurcation (Fig 12D). The resonant behavior is less visible in Fig 12B than in Fig 11 D because the hyperpolarizing step is applied at I_1, which lies further from the Hopf bifurcation than the current used in Fig 11 D. The two channel combinations thus differ not only in bistability window size and robustness, but also in the type of excitability they support: plateau-generating in CaL + Kir and tonic firing with resonant behavior in CaL + KM. In CaL + Kir, the plateau directly reflects resting state robustness: the larger the voltage separation between resting and spiking, the harder it is for noise to drive the neuron out of rest and back into spiking. This separation is largest near I_1 and shrinks toward I_2, consistent with the current-dependent reachability and robustness observed in Fig 7A and Fig 6C vs Fig A in S5 Appendix. In CaL + KM, the Hopf bifurcation eliminates this voltage separation and confers resonator behavior, both of which contribute to the lower robustness and reachability of the resting state compared to CaL + Kir, especially near the Hopf bifurcation (Figs 6, 7, and Fig A in S5 Appendix). The shared SH bifurcation at spiking onset in both cases also provides further insight into the asymmetric shift of I_1 and I_2 induced by Kir and KM channels. The spiking scenario discussed earlier depends on the membrane potential at which the saddle point lies, which is always higher than the resting equilibrium at I_2, supporting the conclusion that the outward Kir (resp. KM) current contribution at I_1 is lower (resp. higher) than at I_2, thereby increasing (resp. decreasing) ΔI.

Discussion

Cooperation between L-type calcium (CaL) channels and inward rectifier potassium (Kir) channels produces a bistability between resting and spiking states that is physiological, robust to noise and intrinsic variability, and capable of supporting plateau potentials and sustained afterdischarges. This combination provides a candidate intrinsic pathway by which deep dorsal horn projection neurons amplify nociceptive input during central sensitization. Our analysis also shows why this pair is special: Kir channels are unusual among voltage-gated potassium channels in that their outward steady-state current, like the CaL inward current, has a region of negative differential conductance around the spike threshold, the same shape feature that enlarges the bistability window.

Most voltage-gated potassium channels reduce the bistability window size in exchange for redressing the resting equilibria within the window, producing the trade-off that has made physiological bistability via CaL channels alone hard to explain [13,19,20]. Kir channels avoid this trade-off through the negative slope of their outward current, which asymmetrically shifts the boundary behaviors of the bistability window to expand it, while anchoring the resting equilibria below the local negative-slope region that Kir channels introduce in the sum of ionic currents. The result is that the region of parameter space where bistability is both robust and physiological is larger for CaL + Kir than for CaL + KM, even though physiological bistability is achievable with either channel combination given sufficient CaL conductance. Selectively blocking either the inward or the outward Kir current reinforces this picture: the inward component exclusively redresses subthreshold resting equilibria, while the outward component alone is responsible for enlarging the bistability window. This clarifies a proposal by Amarillo and colleagues [27] that Kir channels support intrinsic bistability, and generalizes it beyond thalamocortical neurons. The bifurcation analysis tells the same story. Both CaL and Kir channels produce a saddle-node + saddle-homoclinic structure, with Kir channels shifting the saddle point outside the spiking limit cycle range and thereby creating a plateau that separates resting from spiking. KM channels, by contrast, drive the resting equilibrium through a Hopf bifurcation, preventing such a separation.

These functional differences translate into distinct modes of bistability with different implications for neuronal computation. In CaL + Kir bistability, resting and spiking are comparably robust to noise at the center of the bistability window, allowing a projection neuron to reliably hold either state and transition between them under stimulus control. CaL + KM bistability, by contrast, features robust spiking but fragile resting, so once the neuron begins spiking, it tends to remain in that state. This asymmetry is consistent with the Hopf-type loss of stability of the KM resting equilibrium and with our reachability analysis, which showed that the CaL + KM resting state near I_2 is accessible only from a narrow band of initial conditions, becoming increasingly fragile as the applied current approaches I_2. Near I_1, the resting state of CaL + KM becomes more robust than spiking, but both states show comparable robustness, so spiking remains generally dominant throughout the bistability window. For pain processing, where afterdischarges must eventually terminate to allow the system to return to baseline between stimuli, CaL + Kir is therefore the functionally more appropriate mechanism. This conclusion is further supported by our finding that CaL + Kir bistability is more reliable than CaL + KM bistability across a heterogeneous neuronal population exhibiting intrinsic bistability.

The occurrence of long-lasting afterdischarges depends critically on whether the baseline current between pulses falls within the bistability window. Modulatory inputs that shift the window boundaries can therefore gate afterdischarge occurrence: if the window shifts upward (e.g., due to increased $\bar{g}_{\mathrm{Kir}}$), a fixed baseline current may fall below I_1, preventing afterdischarges. Conversely, if the window shifts downward (e.g., due to decreased $\bar{g}_{\mathrm{Kir}}$), the same baseline current may fall within the window, facilitating them. These predictions are consistent with the experimental findings of [6].

The absolute size of the bistability window matters equally for observing long-lasting afterdischarges, but it has not been directly quantified experimentally. However, studies using rats typically applied current pulses of 20 to 150 pA [4,6,15,16], suggesting that the bistability window in these preparations falls within this range. Based on the estimated soma diameter of deep dorsal horn projection neurons of 20 μm [6], this corresponds to approximately 1.6 to 11.9 μA/cm^2, consistent with the range over which we defined our robust-bistability criterion in the minimal model. The upper bound remains less constrained and would require direct experimental measurements of I_1 and I_2. The resting states and firing frequencies observed experimentally could provide additional information to estimate the physiological range of bistability window sizes. However, these properties depend strongly on the full set of ionic conductances present in the neuronal membrane, making it difficult to infer physiological window sizes from a conductance-based model alone.

The firing frequencies in the bistability window of the minimal model (100 to 200 Hz) exceed those reported experimentally for deep projection neurons (5 to 20 Hz) [3,4,6,15,16]. To assess whether this discrepancy limits the applicability of our results, we repeated the analysis of bistability in a two-compartment model of deep projection neurons incorporating additional ion channels [29], which produced firing frequencies more consistent with the experimentally reported range

of 5 – 20 Hz [33]. This supports the generalizability of our findings to more comprehensive models and their robustness to the presence of additional conductances. The other ion channels may further modulate the bistability window. CAN channels have been linked to afterdischarge maintenance [15,29,34,35] and may therefore also promote bistability. KCa channels, which contribute to afterdischarge termination [15] and oppose CaL channel effects on excitability [13,30], may reduce the bistability window and could account for the termination of persistent firing. The faster CaL subtype (CaL, f) enlarged the window much less than the slower subtype in the minimal model (S6 Appendix), suggesting that channel timescale matters as much as channel type. Finally, both CaL and CAN channels have been associated with windup [29,34–36], a form of short-term sensitization in projection neurons. Whether windup shares a mechanistic basis with bistability remains an open question.

In the dorsal horn, Kir channels are modulated by several signaling cascades, including GABA binding to $GABA_B$ receptors, neuropeptide Y (NPY) binding to its Y1 receptor, and gastrin-releasing peptide (GRP) binding to its receptor (GRPR) [37–39]. Bistability may therefore be a more general feature of dorsal horn circuitry, not restricted to projection neurons but potentially extending to interneuron populations that co-express Kir and calcium channels and are targeted by these signaling pathways. In this context, the persistent depolarization and spontaneous activity observed for minutes after synaptic stimulation in GRPR-expressing interneurons [39] may reflect underlying bistability. More broadly, Kir-supported bistability at the single-cell level may be useful wherever a neuron must retain a short-term memory of past input, as noted in thalamocortical and other systems [26–28].

In summary, a minimal conductance-based model shows that CaL and Kir channels cooperate to produce robust and physiological bistability, plateau potentials, and sustained afterdischarges in deep dorsal horn projection neurons. The mechanism relies on a shape feature shared by both steady-state currents, namely a region of negative differential conductance around the spike threshold, which enlarges the bistability window without compromising the physiological plausibility of resting states. Because Kir channels are regulated by multiple neuromodulatory inputs in the dorsal horn, the CaL + Kir pathway is a plausible intrinsic target by which central sensitization switches the functional state of nociception.

Materials and methods

Software

All simulations and experiments were performed in the Julia programming language. The code and packages used in this work are available on GitHub.

Minimal conductance-based model

We used a single-compartment Hodgkin-Huxley model, in which the membrane potential V evolves in response to an applied current I according to:

$$C\frac{dV}{dt} = -I_{\text{leak}} - \sum_{\text{ion}\in\mathcal{I}} I_{\text{ion}} + I, \tag{1}$$

where C is the membrane capacitance, I_{leak} is the leak current, I_{ion} are the intrinsic ionic currents with $\mathcal{I}$ the set of all ionic channels. In this work, the ionic currents flowing in each type of voltage-dependent ion channels are defined by:

$$I_{\text{ion}} = \bar{g}_{\text{ion}}\, m_{\text{ion}}^{q_{\text{ion}}}\, h_{\text{ion}}^{r_{\text{ion}}}\, (V - E_{\text{ion}}), \tag{2}$$

where $\bar{g}_{\text{ion}}$ denotes the ion channels maximal conductance, m_{ion} and h_{ion} correspond to the voltage-dependent activation and inactivation gates of the ion channels, q_{ion} is an integer between 1 and 4, r_{ion} is an integer between 0 and 1, and E_{ion} denotes the reversal potential of the considered ionic current.

The L-type calcium channels, embedding a calcium-dependency, were modeled using a Goldman–Hodgkin–Katz formalism [40] such that:

$$I_{CaL} = \bar{p}_{CaL}\, m_{CaL}^2\, h_{CaL}\, \mathrm{GHK}(V, \left[Ca^{2+}\right]_i), \tag{3}$$

with

$$\mathrm{GHK}(V, \left[Ca^{2+}\right]_i) = 10^{-3} \cdot 2F \cdot \left(\left[Ca^{2+}\right]_i \cdot \frac{-w}{e^{-w}-1} - \left[Ca^{2+}\right]_o \cdot \frac{w}{e^{w}-1} \right), \tag{4}$$

and

$$w = 10^{-3} \cdot V \cdot \frac{2F}{RT}, \tag{5}$$

where F is the Faraday constant, R is the perfect gas constant, T is the temperature, $\left[Ca^{2+}\right]_i$ is the intracellular calcium concentration, and $\left[Ca^{2+}\right]_o$ is the extracellular calcium concentration, considered constant.

The evolution of the intracellular calcium concentration was modeled as:

$$\frac{d\left[Ca^{2+}\right]_i}{dt} = -10^7 \cdot \frac{I_{CaL}}{10^3} \cdot \frac{1}{2Fd} + \frac{\left(\left[Ca^{2+}\right]_{i,0} - \left[Ca^{2+}\right]_i \right)}{\tau_{Ca}}, \tag{6}$$

where I_{CaL} is the intrinsic ionic current flowing in the L-type calcium channels F is the Faraday constant, d is the depth of the shell beneath the membrane, $\left[Ca^{2+}\right]_{i,0}$ is the initial intracellular calcium concentration, and τ_{Ca} is the buffering time constant.

The evolutions of the activation and inactivation gates of a given ion channel are defined as:

$$\begin{aligned} \frac{dm_{ion}}{dt} &= \left(m_{ion,\infty}(V) - m_{ion}\right) / \tau_{m_{ion}}(V), \\ \frac{dh_{ion}}{dt} &= \left(h_{ion,\infty}(V) - h_{ion}\right) / \tau_{h_{ion}}(V), \end{aligned}$$

where $m_{ion,\infty}(V)$ and $h_{ion,\infty}(V)$ denote the steady-state values of the activation and inactivation gates at a given membrane potential V, and $\tau_{m_{ion}}(V)$ and $\tau_{h_{ion}}(V)$ the time constants of the activation and inactivation gates at a given membrane potential V, respectively.

The minimal model includes a voltage-gated fast sodium current I_{Na}, a slow delayed-rectifier potassium current I_{KDR}, an L-type calcium current I_{CaL}, an M-type potassium current I_{KM}, an inward rectifier potassium current I_{Kir}, and a leak current I_{leak}. The models of I_{Na} and I_{KDR} follow [41]. The model of I_{CaL} corresponds to the slower L-type calcium current of [29], with its steady-state activation slightly modified to follow a Boltzmann equation; the faster L-type calcium current, used only in the Appendix, is described there. The models of I_{Kir} and I_{leak} are also from [29]. The model of I_{KM} follows [42], with the half-activation voltage lowered to -76 mV and the slope factor increased to 25.7 mV. These modifications bring the activation range of KM closer to that of Kir, to better contrast their effects. An unmodified version is used in the Appendix and yields the same conclusions (see S7 Appendix).

Throughout, ionic currents are expressed in μA/cm^2, maximal conductances in mS/cm^2, the L-type calcium permeability in cm s^{-1}, calcium concentrations in mM, the membrane potential in mV, and time in ms. Time constants, steady-state

activations, and inactivations for I_{CaL}, I_{KM}, and I_{Kir} are given in Table 1. The nominal values of the fixed parameters are given in Tables 2 and 3.

Complete conductance-based model

To compute the results shown in Fig 5, we reimplemented a published two-compartment conductance-based model of deep projection neurons (see [29] for more details). The ion currents and the fixed parameters described in the previous section are identical to those used in the two-compartment model. This model includes two types of L-type voltage-gated calcium channels as described in [29]. The CaL current described in the previous section corresponds to the slower type, denoted "CaLs" in this paper. In addition, the two-compartment model includes calcium-dependent potassium (KCa) channels and calcium-dependent nonspecific cation (CAN) channels.

Current step and current pulse simulations

A time-dependent applied current was used to observe the neuron response to a current step and pulse. To create a step of current, the time dependency was introduced such that the applied current I is equal to:

$$I(t) = I_{s0} + (I_{s1} - I_{s0})H(t - t_{step}), \tag{7}$$

where $H(x)$ is the unit step function such that it equals 1 if $x \geq 0$ and 0 if $x < 0$. This current step was depolarizing when $I_{s1} > I_{s0}$ and hyperpolarizing otherwise.

To create a pulse of current, the time dependency was introduced such that the applied current I is equal to:

$$I(t) = I_{p0} + (I_{p1} - I_{p0})[H(t - t_{p,starts}) - H(t - t_{p,ends})], \tag{8}$$

Table 1. Steady-state activations and inactivation used to model I_{CaL}, I_{Kir}, and I_{KM}.

x_{ion}	$x_{ion,\infty}(V)$	$\tau_{x_{ion}}(V)$	q_{ion}	r_{ion}
m_{CaL}	$\frac{1}{1+\exp(-(V+25.4)/6)}$	$\frac{160}{\frac{0.1(-V-40)}{\exp(0.1(-V-40))-1}+4\exp((-V-65)/18)}$	/	/
h_{CaL}	$\frac{1}{1+\exp((V+14)/4.03)}$	10000	/	/
m_{Kir}	$\frac{1}{1+\exp((V+65)/10)}$	1	1	0
m_{KM}	$\frac{1}{1+\exp((-V-76,1)/25,7)}$	103	1	0

https://doi.org/10.1371/journal.pcbi.1014549.t001

Table 2. Nominal values of the fixed parameters of the conductance-based model.

C	E_{Na}	E_K	E_{leak}	$\bar{g}_{Na}$	$\bar{g}_{KDR}$	g_{leak}
1 μF/cm^2	50 mV	-90 mV	-60.1 mV	30 mS/cm^2	4 mS/cm^2	0.033 mS/cm^2

https://doi.org/10.1371/journal.pcbi.1014549.t002

Table 3. Nominal values of the fixed parameters of the conductance-based model.

F	R	T	d	τ_{Ca}	$[Ca^{2+}]_o$	$[Ca^{2+}]_{i,0}$
96 520 C mol^{-1}	8.31 J mol^{-1} K	309.15 K	1 nm	10 ms	2 mM	5×10^{-5} mM

https://doi.org/10.1371/journal.pcbi.1014549.t003

meaning that this current pulse was depolarizing when $I_{p1} > I_{p0}$ and hyperpolarizing otherwise.

Both protocols probe bistability. In the step protocol, ascending steps from rest and descending steps from spiking to the same final currents reveal the bistability window by showing which currents lead to different final states depending on initial conditions (Figs 1A–1B). In the pulse protocol, a depolarizing pulse with baseline $I_1 < I_{p0} < I_2$ and amplitude above I_2 triggers a transition to spiking that terminates when the pulse ends, tracing the same window boundaries (Figs 2A,2D). We use the step protocol for parameter sweeps and the pulse protocol to illustrate afterdischarges.

In Fig 1A, we applied four hyperpolarizing steps of current at t_{step} = 250 ms with I_{s0} =-3 μA/cm^2 and I_{s1} taking one of the four values in the ensemble {–2.5; –1.5; –0.5; 0.5} μA/cm^2 from bottom to top. In Fig 1B, we applied four depolarizing steps of current at t_{step} = 250 ms with I_{s0} =1 μA/cm^2 and I_{s1} taking one of the four values in the ensemble {–2.5; –1.5; –0.5; 0.5} μA/cm^2 from bottom to top. For Figs 1A and 1B, we used $\bar{p}_{CaL} = 1.5 \times 10^{-5}$ cm s^{-1} and $\bar{g}_{KM} = \bar{g}_{Kir} = 0$.

In Fig 2A, we applied a depolarizing pulse of current from $t_{p,starts}$ = 250 ms to $t_{p,ends}$ = 350 ms with I_{s0} =1 μA/cm^2 and I_{s1} = 4 μA/cm^2 to the model defined by the set of maximal conductances: $\bar{p}_{CaL} = 1.5 \times 10^{-5}$ cm s^{-1}, $\bar{g}_{KM}$ = 0.15 mS/cm^2, and $\bar{g}_{Kir}$ = 0 mS/cm^2. In Fig 2D, the same depolarizing pulse of current was adapted such that I_{p0} =-0.8 μA/cm^2 and I_{p1} = 2.2 μA/cm^2 to the model defined by the set of maximal conductances: $\bar{p}_{CaL} = 1.5 \times 10^{-5}$ cm s^{-1}, $\bar{g}_{KM}$ = 0 mS/cm^2, and $\bar{g}_{Kir}$ = 0.1 mS/cm^2.

In Fig 5A-5D, we applied several depolarizing pulses of current from $t_{p,starts}$ = 500 ms to $t_{p,ends}$ = 2000 ms. The values of I_{p0}, I_{p1}, $\bar{p}_{CaL}$ and $\bar{g}_{Kir}$ used are given in the bottom part of each of these figures.

In Fig 11, a hyperpolarizing step was applied at t_{step} = 4 s around I_1, with $I_{s0} = I_1 + 10$ nA/cm^2 and $I_{s1} = I_1 - 10$ nA/cm^2 for each set of conductances. Panel A used $\{I_{s0}; I_{s1}\}$ = {–0.05; –0.07} μA/cm^2 and $\{\bar{p}_{CaL}; \bar{g}_{KM}; \bar{g}_{Kir}\}$ = {0.; 0.; 0.}; panel B used {–0.42; –0.44} and {7.5 × 10^{-6} ; 0.; 0.}; panel C used {3.6;3.58} and {0.;0.;0.3}; panel D used {6.6;6.58} and {0.;0.3;0.}. The same step protocol was applied in Fig 12A–12B: panel A used {2.86;2.84} and {7.5 × 10$_{-6}$; 0.; 0.3}; panel B used {6.05;6.03} and {7.5 × 10$_{-6}$; 0.3; 0.}.

Computation of the frequency-current curves

A frequency-current (fI) curve represents the steady-state spiking frequency observed at a constant applied current. In the context of a bistable neuron, an overlap exists between a zero-frequency state (*i.e.*, a resting state) and a non-zero-frequency state (*i.e.*, a spiking state) within a range of current values in which bistability is observed. In this work, we designate this range of current the *bistability window*, which is defined between the onset of spiking at current I_1 and the cessation of resting at I_2.

Thus, the initial conditions used when computing the steady-state spiking frequency for currents within the bistability window must allow the neuron to converge to its spiking state. To determine them, we initialized the neuron at resting and applied a depolarizing current step from the i^{th} current (in the range of current tested) to a higher current, out of the bistability window. Then, the final state observed was used as the initial conditions to simulate the i^{th} constant current and determine the corresponding steady-state spiking frequency. This ensures that the ultra-slow inactivation gate of calcium channels is still open, and facilitates the convergence toward spiking, even with low steady-state frequencies. The model is then simulated for windows of 120 s until the spiking frequency reaches steady-state. To compute the line of zero-frequency of the fI curve, we computed the model fixed points and incorporated a zero-frequency point if a stable fixed point was identified. The combination of these 2 computations was used in Fig 1C (top) and Figs 2B and 2E. In Fig 1C (top), we used the maximal conductances: $\bar{p}_{CaL} = 1.5 \times 10^{-5}$ cm s^{-1} and $\bar{g}_{KM} = \bar{g}_{Kir}$ = 0 mS/cm^2, and a range of applied current between −2.65 and 1 μA/cm^2, with a total of 129 points. In Fig 2B, the maximal conductance $\bar{g}_{KM}$ was increased to 0.15 mS/cm^2, with $\bar{p}_{CaL} = 1.5 \times 10^{-5}$ cm s^{-1} and $\bar{g}_{Kir}$ = 0 mS/cm^2, and a range of applied current between 0.7 and 4 μA/cm^2, with a total of 125 points. Similarly, the conductance $\bar{g}_{Kir}$ was increased to 0.15 mS/cm^2 in Fig 2E, with $\bar{p}_{CaL} = 1.5 \times 10^{-5}$ cm s^{-1} and $\bar{g}_{KM}$ = 0 mS/cm^2, and a range of applied current between −1.1 and 2.4 μA/cm^2, with a total of 127 points.

In Fig 4C, the minimal model was used with $\bar{p}_{CaL} = 1.5 \times 10^{-5}$ cm s^{-1} and three $\{\bar{g}_{KM}; \bar{g}_{Kir}\}$ pairs (in mS/cm^2): {0.02;0.28} (pink, 0.6–5.6 μA/cm^2, 133 points), {0.28;0.02} (purple, 3.9 – –9.9 , 132 points), and {0.28;0.28} (yellow, 6.6 – –9.8 , 120 points).

In Fig 5E,5F (top), the complete model was used with four $\{\bar{p}_{CaL}; \bar{g}_{Kir}\}$ pairs: $\{2.0 \times 10_{-6}; 0.015\}$ (blue, 5 – –250 pA, 1030 points), $\{2.0 \times 10_{-6}; 0.185\}$ (pink, 161–250, 893 points), $\{1.5 \times 10_{-5}; 0.015\}$ (orange, −134–149, 1038 points), and $\{1.5 \times 10_{-5}; 0.185\}$ (green, 14–247, 1028 points).

In Fig 1C (bottom), and Figs 2C and 2F, we also represented the resting equilibria observed for the range of current used to display the fI curve. The resting equilibria were computed together with the line of zero-frequency, by computing the membrane potential associated with the stable fixed point identified for an input range of applied current. The maximal conductances used in Figs 1C (bottom), 2C and 2F were identical to the maximal conductances used in Figs 1C (top), 2B and 2E, respectively. Because the computation of the resting equilibria was much faster than the computation of the fI curve, we were able to use an even more refined range of current for these figures. Indeed, we used a range of applied current between −3 and −0.1 μA/cm^2 with a total of 8914 points for Fig 1C (bottom), between 0 and 3 μA/cm^2 with a total if 2273 points for Fig 2C, and between −1.6 and 1.7 μA/cm^2 with a total of 2920 points for Fig 2E. Note that there were no stable fixed points existing above these ranges of current.

In Fig 4C(bottom), the curves defining the resting equilibrium observed for a given current were computed on ranges of current between 0 and 3.6 μA/cm^2 with a total of 2207 points for the pink curve, between 0 and 6.2 μA/cm^2 with a total of 2278 points for the purple curve, and between 0 and 8.8 μA/cm^2 with a total of 2989 points for the yellow curve. The set of conductances used are identical to those used in Fig 4C(top) for each color.

In Fig 5E–5F(bottom), the curves defining the resting equilibrium observed for a given current were computed on ranges of current between −150 and 55 pA with a total of 492 points for the blue curve, between −150 and 212 pA with a total of 284 points for the pink curve, between −150 and 212 pA with a total of 283 points for the green curve, and between −150 and 49 pA with a total of 480 points for the orange curve. The set of conductances used are identical to those used in Fig 5E–5F(top) for each color.

Computation of the bistability window heatmaps

The computation of the fI curve is associated with a given set of conductances. To capture the evolution of the bistability window size, we varied the pair of conductances, $\bar{p}_{CaL}$ and either $\bar{g}_{KM}$ or $\bar{g}_{Kir}$, and computed for each pair of conductances the (absolute) size of the bistability window, noted:

$$\Delta I = I_2 - I_1. \tag{9}$$

The current I_2, which marks the end of the bistability window, was determined by identifying the highest current with a stable resting state. The stable resting states were computed using the same methodology to compute the fI curve zero-frequency line.

In contrast to the methodology employed in the computation of the descending fI curve, which determined the steady-state spiking frequency for each current within a specified range, in this instance, only the initial current, I_1, situated at the beginning of the bistability window, was subjected to analysis. To compute I_1 for a given pair of conductances in a reasonable execution time, this algorithm was modified by employing an ascending range of current and initiated at a current from the resting-only regime. In this manner, the current I_1 was still identified as the lowest current at which spiking with a constant frequency can be observed over time intervals of 120 s, and with the same methodology employed to compute the neuron initial conditions (extracted from the end of a pulse simulation). The results of this analysis are shown in Fig 3A. In Fig 3D, we performed the same experiment by varying the maximal conductance $\bar{g}_{Kir}$ instead of $\bar{g}_{KM}$.

Similarly, the resting equilibrium at the beginning of the bistability window ($\overline{V}(I_1)$) was determined as the membrane potential of the stable fixed point exhibited at I_1, following the variation of either pair of conductances ($\bar{p}_{CaL}, \bar{g}_{KM}$) or ($\bar{p}_{CaL}, \bar{g}_{Kir}$). This methodology was used for Fig 3C and Fig 3F, respectively.

The heatmaps shown in Fig 4A–4B and Fig 5G–5I were computed in the same manner as what is described here above, with the minimal model and the complete model, respectively. The conductances $\bar{g}_{KM}$ and $\bar{g}_{Kir}$ were varied in ranges each defined between 0 and 0.3 mS/cm^2 including 31 points (Fig 4A–4B). The conductances $\bar{p}_{CaL}$ and $\bar{g}_{Kir}$ were varied in ranges defined between 0 and $3 \times 10_{-5}$ r cm s^{-1} (with 41 points) and 0 and 0.3 mS/cm^2 (with 31 points), respectively (Fig 5G–5I).

Response to noisy input currents

To evaluate the robustness of resting and spiking within the bistability window, we applied a constant current centered on the window of each pair of conductances and added white noise to the voltage equation. For this purpose, we simulated the ODE described in 1 with additive white noise, following a Normal distribution with zero-mean and a standard deviation of σ. The parameter σ was varied between 0 and 9 mV to modify the noise amplitude. The system of equations formed by this stochastic differential equation and the ordinary differential equation associated with the evolution of the ion channels gates and the intracellular calcium concentration was solved with a fixed time step of 0.01 ms.

In Figs 6A, 6B, 6D and 6E, σ was increased at each time step, for a total simulation time of 5 s. In Figs 6A and 6D, the set of initial conditions of the experiment was the resting state observed in the center of the bistability window of the pair of conductances considered (either ($\bar{p}_{CaL}, \bar{g}_{KM}$) or ($\bar{p}_{CaL}, \bar{g}_{Kir}$), respectively). Reciprocally, in Figs 6B and 6E, the set of initial conditions of the experiment was a point of the spike trajectory obtained after applying the center of the bistability window of the pair of conductances considered (either ($\bar{p}_{CaL}, \bar{g}_{KM}$) or ($\bar{p}_{CaL}, \bar{g}_{Kir}$), respectively), without noise for 80 s, such that spiking has reached steady-state before applying any noise.

In Figs 6C and 6F, we evaluated the global neuron ability to sustain either a resting or a spiking state in the presence of a fixed noise amplitude for each type of bistability, which was produced by coupling either ($\bar{p}_{CaL}, \bar{g}_{KM}$) or ($\bar{p}_{CaL}, \bar{g}_{Kir}$), respectively. To that end, the stochastic model was simulated for a period of 50 s with a constant value of σ and initialized to either the resting or the spiking state, both computed from a 80 s noise-free simulation. If the neuron behavior, initially at resting (resp. spiking) transitioned to spiking (resp. resting) at the end of the simulation, a value of 1 was stored as a marker of this state transition, and 0 otherwise. This experiment was repeated 500 times for each standard deviation value tested. The ability to sustain the initial behavioral pattern was quantified by the *proportion of state transition* and calculated as the mean value of the state transition markers recorded for each of the 500 simulations. Both Figs 6C and 6F display the proportion of state transition given the constant value of σ when the neuron is initially spiking or resting. In Fig 6C, bistability relies on the pair ($\bar{p}_{CaL}, \bar{g}_{KM}$) while in Fig 6F, bistability relies on the pair ($\bar{p}_{CaL}, \bar{g}_{Kir}$).

The two sets of conductances were matched for window size. Fig 6A–6C used $\{\bar{p}_{CaL}; \bar{g}_{KM}; \bar{g}_{Kir}\} = \{1.5 \times 10_{-5}; 0.3; 0\}$, giving $\Delta I = 1.77$ μA/cm^2; Fig 6D–6F used $\{1.16 \times 10_{-5}; 0; 0.3\}$, giving $\Delta I = 1.73$ μA/cm^2.

Assessment of the reachability of the resting and spiking states

To complement our analysis of the robustness of the resting and spiking states within the bistability window for each pair of conductances considered, we assessed the reachability of each state. For that purpose, we simulated the system of ODE described in 1 with a constant value of applied current I sampled from the range $[I_1; I_2]$, delimiting each bistability window obtained with ($\bar{p}_{CaL}, \bar{g}_{KM}$) or ($\bar{p}_{CaL}, \bar{g}_{Kir}$). For each value of I tested, we used a range of initial membrane potential V_0 to define different sets of initial conditions written as:

$$(V_0, m_{ion,\infty}(V_0), h_{ion,\infty}(V_0), ..., \left[Ca^{2+}\right]_0), \qquad \text{with } V_0 \in [-90; -20]\ mV,$$

where each activation and inactivation gate were initialized to the value of their steady-state function in V_0 (*i.e.,* $m_{\text{ion},\infty}(V_0)$ and $h_{\text{ion},\infty}(V_0)$, respectively). The initial calcium concentration $\left[Ca^{2+}\right]_0$ was set to 5×10^{-5} mM. For each set of initial conditions and current, we determined the state toward which the neuron converged to, which was either resting or spiking.

In Fig 7A, the following conductances were used: $\bar{p}_{\text{CaL}} = 1.16 \times 10^{-5}$ cm s^{-1}, $\bar{g}_{\text{KM}} = 0$ mS/cm^2, and $\bar{g}_{\text{Kir}} = 0.3$ mS/cm^2, which created a bistability window of $\Delta I = 1.73$ μA/cm^2 with $I_1 = 1.83$ μA/cm^2 and $I_2 = 3.56$ μA/cm^2. In Fig 7B, the following set of conductances was used $\bar{p}_{\text{CaL}} = 1.5 \times 10^{-5}$ cm s^{-1}, $\bar{g}_{\text{KM}} = 0.3$ mS/cm^2, and $\bar{g}_{\text{Kir}} = 0$ mS/cm^2, which created a bistability window of $\Delta I = 1.77$ μA/cm^2 with $I_1 = 4.67$ μA/cm^2 and $I_2 = 6.44$ μA/cm^2. For both Fig 7A and 7B, we used a range of current from I_1 to I_2 with a step of 0.035 μA/cm^2 such that it contained 50 data points, and a range of V_0 defined between –90 mV and –20 mV with a step of 0.1 mV containing 701 data points.

Robustness to different levels of intrinsic variability

Each pair of conductances $(\bar{p}_{\text{CaL}}, \bar{g}_{\text{KM}})$ or $(\bar{p}_{\text{CaL}}, \bar{g}_{\text{Kir}})$ give rise to two types of bistability. We tested their robustness by measuring the relative change in the bistability window size ΔI for each pair considering neurons with heterogeneous intrinsic membrane properties.

To achieve this, three levels of intrinsic variability were introduced, comprising 10, 20, and 30% in three parameters: the membrane capacitance C, the voltage-gated sodium channels maximal conductance $\bar{g}_{\text{Na}}$, and the leak conductance g_{leak}. Each parameter was randomly chosen in an interval centered on the corresponding nominal value used in the model. More specifically, in the case of a level of 10% of variability, the membrane capacitance was sampled according to a uniform distribution from $C(1-0.1)$ to $C\,(1+0.1)$. The same procedure was repeated to sample $\bar{g}_{\text{Na}}$ and g_{leak}. Subsequently, we computed I_1 and I_2, the limits of the bistability window, using the same algorithm as for the bistability window heatmaps, and computed the relative change in the bistability window size ΔI to its nominal value. This computation was realized for both pairs $(\bar{p}_{\text{CaL}}, \bar{g}_{\text{KM}})$ and $(\bar{p}_{\text{CaL}}, \bar{g}_{\text{Kir}})$. The results of the KM model (in purple tones) and the Kir model (in pink tones) in Fig 8 were obtained with the sets of conductances $\{\bar{p}_{\text{CaL}}; \bar{g}_{\text{KM}}; \bar{g}_{\text{Kir}}\} = \{1.5 \times 10^{-5}; 0.3; 0\}$ and $\{\bar{p}_{\text{CaL}}; \bar{g}_{\text{KM}}; \bar{g}_{\text{Kir}}\} = \{1.5 \times 10^{-5}; 0; 0.3\}$, respectively.

Computation of the steady-state currents and the differential conductances

Fig 9 (top) illustrates the steady-state currents of I_{CaL}, I_{KM}, and I_{Kir}. At a given membrane potential, these steady-state currents are defined by the current amplitude with the activation and inactivation gates at steady-state, that is:

$$I_{\text{ion},\infty}(V) = \bar{g}_{\text{ion}} \left(m_{\text{ion},\infty}(V)\right)^{q_{\text{ion}}} \left(h_{\text{ion},\infty}(V)\right)^{r_{\text{ion}}} (V - E_{\text{ion}}), \tag{10}$$

for voltage-dependent ion channels, and

$$I_{\text{CaL},\infty}\left(V, \left[Ca^{2+}\right]_i\right) = \bar{p}_{\text{CaL}}\, m^2_{\text{CaL},\infty}(V)\, h_{\text{CaL},\infty}(V)\, \text{GHK}(V, \left[Ca^{2+}\right]_i), \tag{11}$$

for the L-type calcium channels.

Based on this definition, the differential conductance shown in Fig 9 (bottom) is the derivative of the steady-state current to the membrane potential $(\partial I_{\text{ion},\infty}/\partial V)$ (method inspired from [30]). Each derivative of the steady-state ionic currents were computed with an Euler method, and the intracellular calcium concentration was set to a constant. In Fig 9, we used $\left[Ca^{2+}\right]_i = \left[Ca^{2+}\right]_o$.

Analysis of the contribution of inward and outward currents

To investigate the reasons behind the differing impacts of KM and Kir channels on the bistability window size, we modified these channels separately to block their outward (resp. inward) currents. This approach allowed us to analyze the

contribution of their inward (resp. outward) currents alone. The resulting inward currents flowing in these modified channels are designated by $I_{KM,inward}$ and $I_{Kir,inward}$, while the outward currents are denoted $I_{KM,outward}$ and $I_{Kir,outward}$. This modification is applied to the steady-state functions of the activation gates of both KM and Kir channels, both defined without an inactivation gate, realized as follows:

$$m_{ion,inward,\infty}(V) = \begin{cases} m_{ion,\infty}(V), & \text{if } V \leq E_K, \\ 0, & \text{otherwise,} \end{cases}$$
$$\text{and} \quad m_{ion,outward,\infty}(V) = \begin{cases} m_{ion,\infty}(V), & \text{if } V > E_K, \\ 0, & \text{otherwise.} \end{cases} \tag{12}$$

Fig 10 (left) represents the steady-state inward and outward KM and Kir currents. To compute them, we replaced the steady-state activation gates previously used by their inward/outward form, defined above, in the definition of the steady-state currents. In Fig 10 (center), we represented the evolution of the bistability window limits (I_1 and I_2) as the maximal conductance of the current taken into account increased. The same methodology employed for the bistability window heatmaps was used to compute those limits. In Fig 10 (right), we applied hyperpolarizing steps of currents to a neuron with a fixed maximal conductance for the current considered (*i.e.*, the inward KM current in the case of Fig 10A (right) from I_2 to I_1, with t_{step} = 250 ms, starting from the resting state in I_2, for a total time of 1 s. The permeability $\bar{p}_{CaL}$ used in Fig 10 was 1.5×10^{-5} cm s^{-1}.

Bifurcation analyses around the excitability switches

In Figs 11E–11H and Figs 12C–12D, we computed bifurcation diagrams with respect to the applied current *I*. Fixed points were computed with the `NLsolve` package for each tested *I*. Limit-cycle extrema during spiking were computed using the same methodology as for the fI curves. Conductance sets used (as $\{\bar{p}_{CaL}; \bar{g}_{KM}; \bar{g}_{Kir}\}$): Fig 11 E, {0.;0.;0.}; Fig 11 F, $\{7.5 \times 10^{-6}; 0.; 0.\}$; Fig 11 G, {0.;0.;0.3}; Fig 11 H, {0.;0.3;0.}; Fig 12C, $\{7.5 \times 10^{-6}; 0.; 0.3\}$; Fig 12D, $\{7.5 \times 10^{-6}; 0.3; 0.\}$.

Supporting information

S1 Appendix. S1 Appendix.
(PDF)

S2 Appendix. S2 Appendix.
(PDF)

S3 Appendix. S3 Appendix.
(PDF)

S4 Appendix. S4 Appendix.
(PDF)

S5 Appendix. S5 Appendix.
(PDF)

S6 Appendix. S6 Appendix.
(PDF)

S7 Appendix. S7 Appendix.
(PDF)

Author contributions

Conceptualization: Anaëlle De Worm, Guillaume Drion, Pierre Sacré.

Data curation: Anaëlle De Worm.

Formal analysis: Anaëlle De Worm, Guillaume Drion, Pierre Sacré.

Investigation: Anaëlle De Worm.

Methodology: Anaëlle De Worm, Guillaume Drion, Pierre Sacré.

Project administration: Anaëlle De Worm.

Resources: Anaëlle De Worm.

Software: Anaëlle De Worm.

Supervision: Guillaume Drion, Pierre Sacré.

Validation: Anaëlle De Worm.

Visualization: Anaëlle De Worm.

Writing – original draft: Anaëlle De Worm.

Writing – review & editing: Anaëlle De Worm, Guillaume Drion, Pierre Sacré.

References

1. Woolf CJ. What is this thing called pain?. J Clin Invest. 2010;120(11):3742–4. https://doi.org/10.1172/JCI45178 PMID: 21041955
2. Latremoliere A, Woolf CJ. Central sensitization: a generator of pain hypersensitivity by central neural plasticity. J Pain. 2009;10(9):895–926. https://doi.org/10.1016/j.jpain.2009.06.012 PMID: 19712899
3. Reali C, Russo RE. An integrated spinal cord-hindlimbs preparation for studying the role of intrinsic properties in somatosensory information processing. J Neurosci Methods. 2005;142(2):317–26. https://doi.org/10.1016/j.jneumeth.2004.09.006 PMID: 15698671
4. Monteiro C, Lima D, Galhardo V. Switching-on and -off of bistable spontaneous discharges in rat spinal deep dorsal horn neurons. Neurosci Lett. 2006;398(3):258–63. https://doi.org/10.1016/j.neulet.2006.01.008 PMID: 16448752
5. Zain M, Bonin RP. Alterations in evoked and spontaneous activity of dorsal horn wide dynamic range neurons in pathological pain: a systematic review and analysis. Pain. 2019;160(10):2199–209. https://doi.org/10.1097/j.pain.0000000000001632 PMID: 31149976
6. Derjean D, Bertrand S, Le Masson G, Landry M, Morisset V, Nagy F. Dynamic balance of metabotropic inputs causes dorsal horn neurons to switch functional states. Nat Neurosci. 2003;6(3):274–81. https://doi.org/10.1038/nn1016 PMID: 12592405
7. Cata JP, Weng H-R, Chen J-H, Dougherty PM. Altered discharges of spinal wide dynamic range neurons and down-regulation of glutamate transporter expression in rats with paclitaxel-induced hyperalgesia. Neuroscience. 2006;138(1):329–38. https://doi.org/10.1016/j.neuroscience.2005.11.009 PMID: 16361064
8. Robinson CR, Zhang H, Dougherty PM. Altered discharges of spinal neurons parallel the behavioral phenotype shown by rats with bortezomib related chemotherapy induced peripheral neuropathy. Brain Res. 2014;1574:6–13. https://doi.org/10.1016/j.brainres.2014.06.013 PMID: 24949562
9. Lee RH, Heckman CJ. Bistability in spinal motoneurons in vivo: systematic variations in rhythmic firing patterns. J Neurophysiol. 1998;80(2):572–82. https://doi.org/10.1152/jn.1998.80.2.572 PMID: 9705451
10. Kazantsev VB, Asatryan SY. Bistability induces episodic spike communication by inhibitory neurons in neuronal networks. Phys Rev E Stat Nonlin Soft Matter Phys. 2011;84(3 Pt 1):031913. https://doi.org/10.1103/PhysRevE.84.031913 PMID: 22060409
11. Dovzhenok A, Kuznetsov AS. Exploring neuronal bistability at the depolarization block. PLoS One. 2012;7(8):e42811. https://doi.org/10.1371/journal.pone.0042811 PMID: 22900051
12. Engbers JDT, Fernandez FR, Turner RW. Bistability in Purkinje neurons: ups and downs in cerebellar research. Neural Netw. 2013;47:18–31. https://doi.org/10.1016/j.neunet.2012.09.006 PMID: 23041207
13. Franci A, Drion G, Seutin V, Sepulchre R. A balance equation determines a switch in neuronal excitability. PLoS Computational Biology. 2013;9(5):e1003040. https://doi.org/10.1371/journal.pcbi.1003040
14. Borges FS, Protachevicz PR, Souza DLM, Bittencourt CF, Gabrick EC, Bentivoglio LE, et al. The Roles of Potassium and Calcium Currents in the Bistable Firing Transition. Brain Sci. 2023;13(9):1347. https://doi.org/10.3390/brainsci13091347 PMID: 37759949
15. Morisset V, Nagy F. Ionic basis for plateau potentials in deep dorsal horn neurons of the rat spinal cord. J Neurosci. 1999;19(17):7309–16. https://doi.org/10.1523/JNEUROSCI.19-17-07309.1999 PMID: 10460237

16. Reali C, Fossat P, Landry M, Russo RE, Nagy F. Intrinsic membrane properties of spinal dorsal horn neurones modulate nociceptive information processing in vivo: plateau potentials and in vivo nociceptive integration. The Journal of Physiology. 2011;589(11):2733–43. https://doi.org/10.1113/jphysiol.2011.207712
17. Crunelli V, Tóth TI, Cope DW, Blethyn K, Hughes SW. The "window" T-type calcium current in brain dynamics of different behavioural states. J Physiol. 2005;562(Pt 1):121–9. https://doi.org/10.1113/jphysiol.2004.076273 PMID: 15498803
18. Le T, Verley DR, Goaillard J-M, Messinger DI, Christie AE, Birmingham JT. Bistable behavior originating in the axon of a crustacean motor neuron. J Neurophysiol. 2006;95(3):1356–68. https://doi.org/10.1152/jn.00893.2005 PMID: 16291803
19. Yuen GL, Hockberger PE, Houk JC. Bistability in cerebellar Purkinje cell dendrites modelled with high-threshold calcium and delayed-rectifier potassium channels. Biol Cybern. 1995;73(4):375–88. https://doi.org/10.1007/BF00199473 PMID: 7578476
20. Naudin L, Raison-Aubry L, Buhry L. A general pattern of non-spiking neuron dynamics under the effect of potassium and calcium channel modifications. J Comput Neurosci. 2023;51(1):173–86. https://doi.org/10.1007/s10827-022-00840-w PMID: 36371576
21. Murata Y, Yasaka T, Takano M, Ishihara K. Neuronal and glial expression of inward rectifier potassium channel subunits Kir2.x in rat dorsal root ganglion and spinal cord. Neurosci Lett. 2016;617:59–65. https://doi.org/10.1016/j.neulet.2016.02.007 PMID: 26854211
22. Ford NC, Baccei ML. Inward-rectifying K+ (Kir2) leak conductance dampens the excitability of lamina I projection neurons in the neonatal rat. Neuroscience. 2016;339:502–10. https://doi.org/10.1016/j.neuroscience.2016.10.027
23. Malcangio M. GABAB receptors and pain. Neuropharmacology. 2018;136:102–5. https://doi.org/10.1016/j.neuropharm.2017.05.012
24. Brewer CL, Baccei ML. Enhanced Postsynaptic GABAB Receptor Signaling in Adult Spinal Projection Neurons after Neonatal Injury. Neuroscience. 2018;384:329–39. https://doi.org/10.1016/j.neuroscience.2018.05.046 PMID: 29885525
25. Shoemaker PA. Neural bistability and amplification mediated by NMDA receptors: Analysis of stationary equations. Neurocomputing. 2011;74(17):3058–71. https://doi.org/10.1016/j.neucom.2011.04.018
26. Sanders H, Berends M, Major G, Goldman MS, Lisman JE. NMDA and GABAB (KIR) conductances: the "perfect couple" for bistability. J Neurosci. 2013;33(2):424–9. https://doi.org/10.1523/JNEUROSCI.1854-12.2013 PMID: 23303922
27. Amarillo Y, Tissone AI, Mato G, Nadal MS. Inward rectifier potassium current IKir promotes intrinsic pacemaker activity of thalamocortical neurons. J Neurophysiol. 2018;119(6):2358–72. https://doi.org/10.1152/jn.00867.2017 PMID: 29561202
28. Delmoe M, Secomb TW. Conditions for Kir-induced bistability of membrane potential in capillary endothelial cells. Math Biosci. 2023;355:108955. https://doi.org/10.1016/j.mbs.2022.108955 PMID: 36513149
29. Le Franc Y, Le Masson G. Multiple firing patterns in deep dorsal horn neurons of the spinal cord: computational analysis of mechanisms and functional implications. J Neurophysiol. 2010;104(4):1978–96. https://doi.org/10.1152/jn.00919.2009 PMID: 20668279
30. Drion G, Franci A, Dethier J, Sepulchre R. Dynamic Input Conductances Shape Neuronal Spiking. eNeuro. 2015;2(1):ENEURO.0031-14.2015. https://doi.org/10.1523/ENEURO.0031-14.2015 PMID: 26464969
31. Franci A, Drion G, Sepulchre R. An Organizing Center in a Planar Model of Neuronal Excitability. SIAM J Appl Dyn Syst. 2012;11(4):1698–722. https://doi.org/10.1137/120875016
32. Izhikevich EM. Dynamical Systems in Neuroscience: The Geometry of Excitability and Bursting. Sejnowski TJ, Poggio TA. Cambridge, MA, USA: MIT Press. 2006.
33. Zhang TC, Janik JJ, Grill WM. Modeling effects of spinal cord stimulation on wide-dynamic range dorsal horn neurons: influence of stimulation frequency and GABAergic inhibition. J Neurophysiol. 2014;112(3):552–67. https://doi.org/10.1152/jn.00254.2014 PMID: 24790169
34. Fossat P, Sibon I, Le Masson G, Landry M, Nagy F. L-type calcium channels and NMDA receptors: a determinant duo for short-term nociceptive plasticity. Eur J Neurosci. 2007;25(1):127–35. https://doi.org/10.1111/j.1460-9568.2006.05256.x PMID: 17241274
35. Aguiar P, Sousa M, Lima D. NMDA channels together with L-type calcium currents and calcium-activated nonspecific cationic currents are sufficient to generate windup in WDR neurons. Journal of Neurophysiology. 2010;104(2):1155–66. https://doi.org/10.1152/jn.00834.2009
36. Aby F, Bouali-Benazzouz R, Landry M, Fossat P. Windup of Nociceptive Flexion Reflex Depends on Synaptic and Intrinsic Properties of Dorsal Horn Neurons in Adult Rats. Int J Mol Sci. 2019;20(24):6146. https://doi.org/10.3390/ijms20246146 PMID: 31817540
37. Busserolles J, Gasull X, Noël J. Potassium Channels and Pain. The Oxford Handbook of the Neurobiology of Pain. Oxford University Press. 2019. 263–312. https://doi.org/10.1093/oxfordhb/9780190860509.013.19
38. Sinha GP, Prasoon P, Smith BN, Taylor BK. Fast A-type currents shape a rapidly adapting form of delayed short latency firing of excitatory superficial dorsal horn neurons that express the neuropeptide Y Y1 receptor. J Physiol. 2021;599(10):2723–50. https://doi.org/10.1113/JP281033 PMID: 33768539
39. Pagani M, Albisetti GW, Sivakumar N, Wildner H, Santello M, Johannssen HC, et al. How Gastrin-Releasing Peptide Opens the Spinal Gate for Itch. Neuron. 2019;103(1):102-117.e5. https://doi.org/10.1016/j.neuron.2019.04.022 PMID: 31103358
40. Hodgkin AL, Katz B. The effect of sodium ions on the electrical activity of giant axon of the squid. J Physiol. 1949;108(1):37–77. https://doi.org/10.1113/jphysiol.1949.sp004310 PMID: 18128147
41. Destexhe A, Contreras D, Sejnowski TJ, Steriade M. A model of spindle rhythmicity in the isolated thalamic reticular nucleus. J Neurophysiol. 1994;72(2):803–18. https://doi.org/10.1152/jn.1994.72.2.803 PMID: 7527077
42. Miceli F, Soldovieri MV, Ambrosino P, De Maria M, Migliore M, Migliore R, et al. Early-onset epileptic encephalopathy caused by gain-of-function mutations in the voltage sensor of Kv7.2 and Kv7.3 potassium channel subunits. J Neurosci. 2015;35(9):3782–93. https://doi.org/10.1523/JNEUROSCI.4423-14.2015 PMID: 25740509